COT **알고리즘 기술 분석서**
(Algorithm Theoretical Basis Document)

NMSC/SCI/ATBD/COT, Issue 1, rev.4
2012.12.26

국가기상위성센터

REPORT SIGNATURE TABLE

Function	Name	Signature	Date
Prepared by	최용상, 조희제		2012.12.26
Reviewed by	최용상		2012.12.26
Authorised by	국가기상위성센터		2012,12.26

DOCUMENT CHANGE RECORD

Version	Date	Pages	Changes
Version4	2012.12.26	-	-ATBD 형식 외에 내용이 바뀐 부분은 없음

차 례

List of Tables

List of Figures

List of Acronyms

COMS	Communication, Ocean, and Meteorological Satellite
MTSAT	Multi-functional Transport Satellite
JAMI	Japanese Advanced Meteorological Imager
ISCCP	International Satellite Cloud Climatology Project
SOBS	Gridded surface weather station reports
FOV	Field of view
MODIS	Moderate Resolution Imaging Spectroradiometer
COT	Cloud Optical Depth
ER	Effective Radius
SBDART	Santa Barbara DISORT Atmospheric Radiative Transfer

1. 개요

본 알고리즘은 구름광학두께와 유효입자반경을 산출하기 위한 것이다. 자료 산출을 위한 주 입력 자료는 VIS0.65㎛와 SWIR3.75㎛ 복사휘도이다. 본 알고리즘은 0.65㎛ 채널의 특성상 주간의 경우에만 구름광학두께의 산출이 가능하다. VIS0.65㎛는 지표반사도에 영향을 받으므로 지표반사도가 구름광학두께와 유효입자 반경을 산출함에 있어 매우 중요하다. 주간의 경우 SWIR3.75 ㎛에는 지구복사성분이 포함 된다. 이를 제거하기 위해 IR10.8㎛ 복사휘도를 이용한다. 이렇게 보정한 VIS0.65㎛와 SWIR3.75㎛ 복사휘도는 복사전달모델을 통해 미리 계산된 조견표와 대응하여 최적의 구름광학두께와 유효입자반경을 동시에 찾는다. 이렇게 산출된 정보는 구름복사 강제력 연구뿐만 아니라 ISCCP 운형 분류에 있어 필수 자료가 된다.

2. 배경 및 목적

구름광학두께 알고리즘은 주간의 구름픽셀에 대해 수행한다. 따라서 태양천정각 검사와 장면 검사가 필요하다. 이는 미리 계산된 결과를 사용한다. 알고리즘에 IR10.8㎛의 복사휘도와 지표반사도를 고려하는 부분이 포함되어 있다. VIS0.65㎛의 경우 지표의 반사도에 영향을 받아 이에 대한 보정이 필요하다. 보정은 간단한 함수에 의해 계산된다. 함수의 상수는 지표반사도에 따라 변하도록 설계하였다. 알고리즘에 사용되는 지표반사도 값은 8일 간격의 공간 해상도가 10 km인 고해상도의 MODIS Terra와 Aqua 알베도 자료를 접합하여 사용하였다. SWIR3.75㎛는 주간의 경우 지구복사와 태양복사 성분을 동시에 포함한다. 지구복사 성분을 IR10.8㎛의 휘도온도에 대한 함수로 처리하여 보정하였다. 조견표의 계산값과 관측값을 대응시켜 최종 산출물은 구름광학두께와 유효 입자반경을 동시에 산출한다.

3. 알고리즘

3.1. 이론적인 배경 및 근거(Theoretical Background)

GMS-5의 경우, 0.6 ㎛의 가시채널만을 사용하여 구름광학두께를 산출한다. 그러나 이 방법은 모든 구름의 유효입자방경을 10 ㎛로 가정하게 된다. 그 뒤로 King(1987)과 Nakajima et al.(1990)에 의해 발전된 구름광학두께 산출 알고리즘은 solar reflectance technique가 개발되었고, 이 방법은 현재 MODIS가 운용중이고 1 km의 공간 해상도로 낮시간만 산출한다. 본 알고리즘 역시 MODIS와 마찬가지로 Solar reflectance technique를

사용하였다. Solar reflectance technique는 가시채널과 근적외채널을 이용한 것으로 수증기의 흡수 여부에 따라 다음과 같이 두 가지로 분류할 수 있다.

가. 수증기 비흡수 영역 : 0.65, 0.86, 1.24 ㎛
나. 수증기 흡수 영역 : 1.6, 2.1, 3.7 ㎛

또한, 지표면의 성질에 따른 수증기의 비흡수 파장대는 다음과 같이 사용한다.
가. 육지 : 0.65 ㎛, 해양 : 0.86 ㎛
나. 눈 / 얼음 : 1.24 ㎛

Fig. 1은 구름광학두께(τ_c = 1, 2, 4, 8, 16, 32, 64)와 유효 반경(r_e = 2, 4, 8, 16, 32)의 함수인 AVHRR 채널 1(0.64 ㎛)과 채널 3(3.75 ㎛)의 태양 반사 복사량의 그래프이다(Nakajima et al., 1995). 이와 같이 수증기 흡수 파장대와 비흡수 파장대에 대한 반사율은 구름광학두께와 유효 입자반경의 크기에 의존한다. 미리 복사전달모델에 의해 계산된 두 영역에서의 반사율은 관측값과 대응되어 최적의 구름광학두께와 유효 입자반경을 찾는다. 그리고 이에 대한 좀 더 자세한 내용은 Appendix (Choi et al. 2007, IJRS)의 4,722~4,725 페이지에 소개되어 있다.

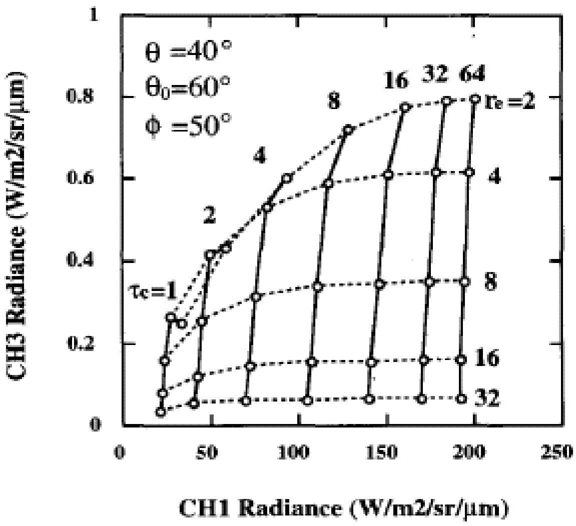

Fig. 1. Comparison of ch1 and ch3 radiances for various cloud optical thicknesses and effective radius values (King et al, 1997).

하지만, 현재의 기술력으로는 낮 시간만 자료 산출이 가능하고, 액체 상 구름에 대해서는 적용되지만 얇은 권운에 대해서는 모호한 결과가 산출되는 문제점이 있다. 지구 전 표면에 대해 수증기 비흡수 파장대인 0.65, 0.86, 1.24 ㎛ 채널은 모두 요구되나, 수증기 흡수 파장대인 근적외선 영역은 1.6 ㎛이나 3.75 ㎛ 중 하나만이 요구된다. 그러나 본 COMS 알

고리즘에서는 가용한 0.675 ㎛를 이용하여 육지, 해양에서의 구름광학두께를 산출하고, 눈이나 얼음으로 덮힌 지면에 대해서는 이의 산출을 생략한다. 현재 ISCCP는 구름의 광학두께를 0.6 ㎛의 반사율만으로 정의하여 생산하므로 최소한 ISCCP 운형분류를 위해서 필요한 자료를 생산할 수 있다. 또한 복사전달모델의 계수를 적절히 선택하지 않으면 정확한 조견표를 얻기 힘들다.

3.2. 산출방법(Methodology)

3.2.1. 조견표 산출 방법

##	
# SBDART input program for COT lookup table	
##	
if [$do4] ; then	
rm -f $root.4	
echo running example 4	Do-loop start!
for albcon in 0 0.5 ; do	A spectrally uniform, surface albedo
for tcloud in 0 2 4 8 16 32 64 128; do	cloud optical thickness
for nre in -2 -4 -8 -16 -32 -64; do	effective radius (positive=water, negative=ice)
for sza in 0 10 20 30 40 50 60 70 80 ;do	solar zenith angle
echo "	
&INPUT	
albcon=$albcon	surface albedo
tcloud=$tcloud	cloud optical thickness
sza=$sza	solar zenith angle
nre=$nre	effective radius
wlinf=0.73	lower wavelength limit
wlsup=0.73	upper wavelength limit
uzen=0,10,20,30,40,50,60,70,80	satellite zenith angle
phi=0	
idatm=2	idatm = 1 for tropical = 2 for mid-latitude summer = 3 for mid-latitude winter
iout=20	Radiance output at TOA km
nothrm=1	1 for no thermal emission
/" > INPUT	
sbdart >> $root.4	

done done done done fi	

구름광학두께와 유효입자반경은 수증기의 흡수 및 비흡수 파장대에서의 반사도의 함수이다. 이 원리를 이용하여 복사전달모델에서 미리 계산된 반사도를 관측값과 대응시켜 최적의 구름광학두께와 유효입자반경을 산출한다. 이를 위해 지표반사도, 구름광학두께, 유효입자반경, 태양천정각과 위성 천정각의 다양한 입력 조건을 가지고 열대지방, 중위도 지역 여름과 겨울에 대해 SBDART 복사전달모델을 수행하였다.

0.65㎛는 지표 반사도에, 3.75㎛ 지구복사 성분에 영향을 받으므로 이에 대한 보정을 고려해야한다. 또한 반사도가 기하학적 관측각과 태양입사각에 따라 상이하므로 이를 반드시 고려해야 한다(Table 1). Table 1은 구름광학두께를 산출하기위한 조견표로 θ_0는 태양천정각, θ는 위성천정각을 나타낸다. 조견표는 IDL program에서 array의 재배열이 이루어지는 형태로, 간단하게 계산된다. IDL 프로그램의 입력 자료는 SBDART를 통해 모의된 다양한 COT, ER에 대해 모의된 3.75㎛, 0.675㎛ 복사휘도이다.

Table 1. Lookup table for COT & ER algorithm.

Land/Sea	θ_0	θ	Rad0.6	Rad3.7	COT	ER
0	35	23	0.12	0.23	45.23	3.23
1	34	23	0.11	0.22	23.42	12.32
0	21	45	0.34	0.45	84.12	21.31
…	…	…	…	…	…	…

주간의 3.75㎛ 복사휘도는 태양복사성분 및 지구복사성분을 동시에 가지고 있다. 그러므로 구름광학두께 산출 시 정확도를 높이기 위해서는 3.75㎛ 복사휘도의 지구복사성분을 제거해야한다. 지구복사성분을 제거하기 위해 10.8㎛ 복사휘도를 이용하였다. Fig. 2는 10.8㎛복사휘도와 3.75㎛의 지구복사성분과의 관계를 나타낸다. 구름광학두께 산출 알고리즘에 관계를 사용하여 3.75㎛의 지구복사성분을 제거하였다.

VIS0.65㎛ 복사휘도는 구름광학두께 및 지표알베도의 함수이다. 복사전달모델을 사용하여 다양한 조건(solar zenith angle: 0~80, solar zenith angle: 0~80, cloud optical thickness: 0~123, effective particle radius: 2~64)에서 지표반사도에 따른 VIS0.65㎛ 복사휘도의 변화를 모의하였다. 지표반사도 효과는 다음과 같은 간단한 함수로 표현할 수 있다.

$$L_{0.65} = a_0 + a_1 L^{obs}_{0.65} + a_2 (L^{obs}_{0.65})^2 \tag{1}$$

여기서 $L_{0.65}$는 보정된 VIS0.65㎛ 복사휘도이고, $L^{obs}_{0.65}$는 관측된 VIS0.65㎛ 복사휘도이다. a_0, a_1, 그리고 a_2 는 계수로 지표반사도에 따라 달라진다. 이를 통해 볼 때 구름광학두께 산출에 지표반사도 효과를 제거하는 것이 산출물의 정확도에 직접적으로 영향을 준다고 할 수 있다.

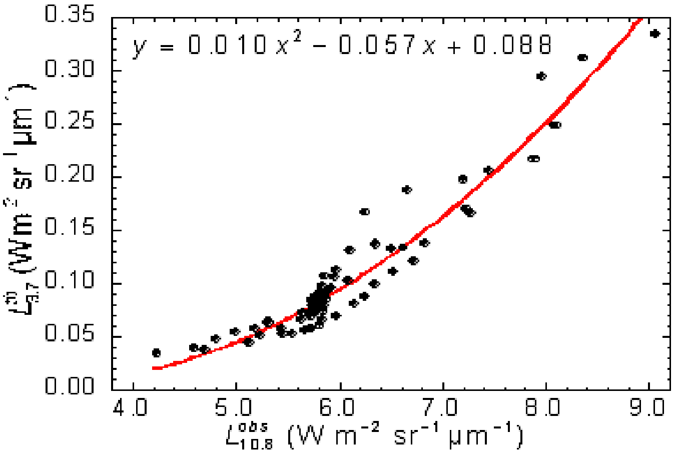

Fig. 2. Sensitivity of SWIR3.7 ㎛ thermal radiances ($L^{th}_{3.7}$) to IR10.8-㎛ satellite-received radiances ($L^{obs}_{10.8}$) for the clouds with a variety of τ_c (0 to 64) and r_e (0 to 32 μm) under diverse Tc and Tg. The solid line is the 2nd-order polynomial regression line of the plots.

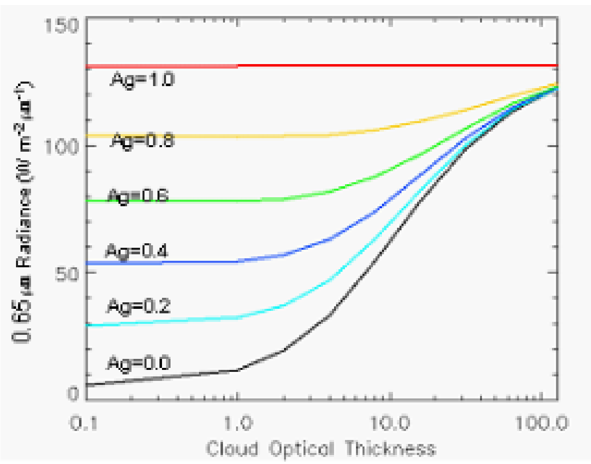

Fig. 3. Simulated radiances in VIS0.65㎛ as a function of cloud optical thickness and surface albedo(Ag).

3.3. 산출과정

3.3.1. 구름광학두께 산출

구름광학두께를 구하기 위한 알고리즘의 흐름도는 Fig. 4와 같다. 장면분석 및 태양천정각 검사 결과를 이용하여 주간의 구름화소인 경우에만 알고리즘을 적용한다. 알고리즘의 첫 단계는 IR10.8㎛의 복사휘도와 지표반사도를 고려하여 VIS0.65㎛와 SWIR3.75㎛의 복사휘도를 보정한다. VIS0.65㎛ 복사휘도 보정에는 지표반사도가, SWIR3.75㎛ 복사휘도 보정에는 IR10.8㎛ 복사휘도가 사용된다. 다음 단계는 보정된 VIS0.65㎛와 SWIR3.75㎛의 복사휘도를 조견표의 계산값에 대응시켜 최종 산출물인 구름광학두께와 유효 입자반경을 동시에 산출하는 것이다. 이 단계에는 구름상 정보가 필요하다. VIS0.65㎛와 SWIR3.75㎛의 복사휘도는 구름상에 영향을 받는다. 조견표는 구름상 정보(얼음상, 물상) 및 태양천정각(0~80°), 위성천정각(0~80°), 지표반사도 (0, 0.5) 고려하여 계산되었다. 본 알고리즘에서 지표반사도를 Choi et al. (2007)에서 제안된 1 대신 0.5를 사용하였는데 그 이유는 실제 Multi-functional Transport Satellite (MTSAT) Field of view (FOV)에서 측정된 실제 지표반사도가 0.5보다 작기 때문이다. 이론적으로 지표면과 상층사이에 매우 작고 복잡한 반사가 일어난다는 가정 하에서는 지표면 복사휘도는 지표반사도에 선형관계가 성립하는데 태양천정각과 위성천정각이 60~80° 일 경우는 이러한 선형관계가 잘 성립하지 않으므로 구름광학두께와 유효입자반경을 산출하는데 제약이 따른다.

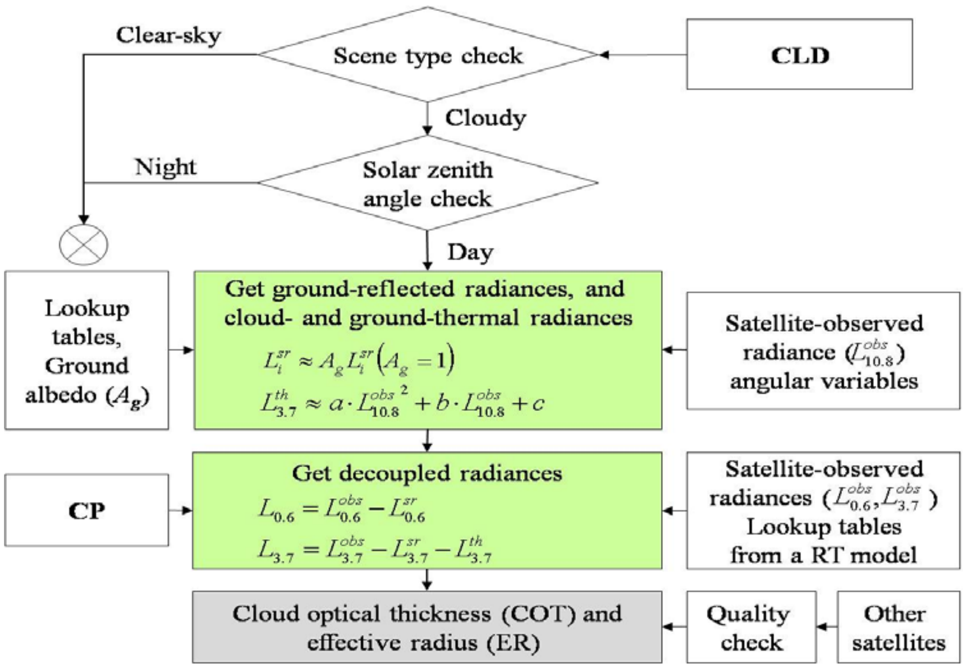

Fig. 4. Flowchart of the COT algorithm.

SWIR3.75㎛채널은 근적외채널로 주간의 경우 태양복사 및 지구복사 효과를 동시에 받는다(Fig. 5). Fig. 5 a)는 SWIR3.75㎛의 지구복사 성분이 없는 경우이고 Fig. 5 b)는 지구복사 성분이 포함되어 있는 경우이다. 이들의 차이는 알고리즘 산출물의 정확도에 영향을 미친다. SWIR3.75㎛의 지구복사 성분을 얼마나 효과적으로 제거하느냐는 산출물의 정확도와 관련이 있다. 본 알고리즘은 IR10.8㎛을 이용하여 이를 제거하였다. IR10.8㎛은 오직 지구복사의 영향만 받는 채널로 이를 이용하여 지구 복사량의 정도를 파악하려는 것이다. 복사 전달 모의 결과 SWIR3.75㎛의 지구복사 성분과 IR10.8㎛의 복사 휘도 사이에는 간단한 함수가 성립한다. 이 함수를 알고리즘에 적용하여 위성에서 관측되는 SWIR3.75㎛의 복사 휘도에서 지구복사 성분을 제거하도록 하였다.

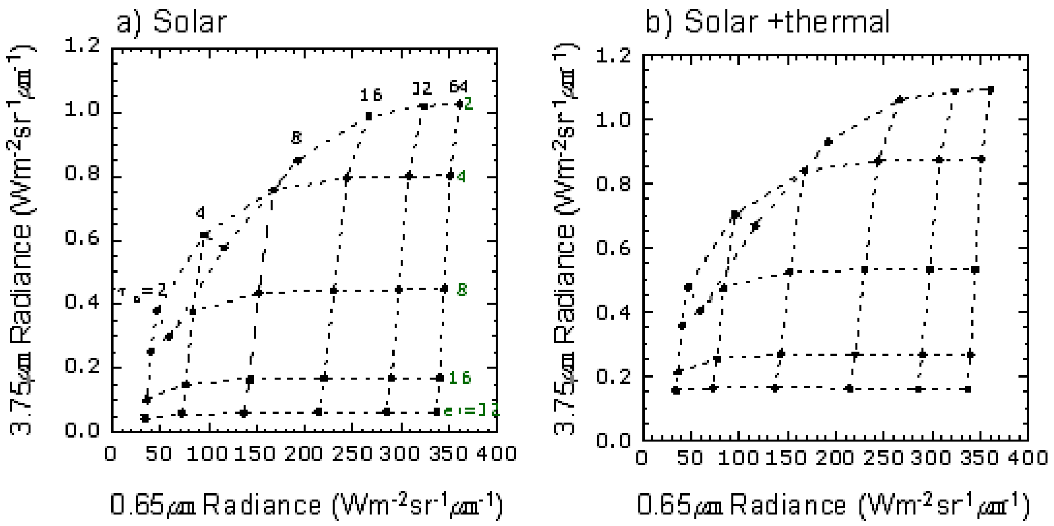

Fig. 5. The relationships between the radiance at 0.65 and 3.75㎛ for values of cloud optical thickness and effective particle radius.

3.3.2. QC flag

구름광학두께에 대한 QC flag가 table 2에 제시 되었다. 크게 4가지로 구분하여 QC flag를 주도록 하였다. 구름 광학두께를 산출함에 있어 지표 알베도가 중요한 요인 중에 하나다. 그러므로 첫 번째 QC flag는 지표 알베도에 대하여 96-240 까지 flag를 주도록 하였다. 두 번째는 구름광학두께의 범위에 따라 50보다 큰 경우와 50과 100 사이 그리고 100보다 클 때에 대하여 각각 flag를 줌으로써 권운인지 아닌지를 판단 할 수 있고, 구름상과 유효입자반경에 대하여 세 번째 flag를 주었다. 그리고 마지막으로 유효입자반경이 산출되지 않는 경우에 대하여 flag를 주도록 설계하였다.

Table 2. QC Flag

CLA - COT		
bit	Bit Interpretation	Field Description
8~5 (Ground albedo used - MOD43C3) unavail => 0	240 224 208 192 176 160 144 128 112 96	0~0.1 0.1~0.2 0.2~0.3 0.3~0.4 0.4~0.5 0.5~0.6 0.6~0.7 0.7~0.8 0.8~0.9 0.9~1
4~3 (Optical Depth Range)	12 8 4 0	0 < COT <= 50 50 < COT < 100 COT > 100 COT = 0
2 (Cloud Phase)	3 2	CP = 1 and ER > 30 CP = 2 and ER < 5
1 (ER=>unavailable)	1	ER in detectable range

3.4. 검증

3.4.1. 검증방법

CMDPS로부터 산출된 구름광학두께는 MODIS 자료를 사용하여 CMDPS에 의한 실시간 검증과 알고리즘의 유효성 여부를 판단하기 위한 개발자에 의해 자체적으로 다양한 방법을 통해 검증이 이루어 졌다. CMDPS 검증은 알고리즘의 정확도 및 유효성을 판단하기 위해 통계학적 방법으로 검증을 하였고, 개발자에 의한 자체 검증은 주로 장면 분석과 기후값에 근거하여 검증을 실시하였다. 유효입자반경은 산출은 되지만 검증의 대상에서는 제외되었다.

3.4.1.1. 검증을 위한 전처리 과정-간소화 된 ISCCP 구름탐지

통신해양기상위성의 모의 영상으로서 MTSAT-1R에 탑재된 Japanese Advanced Meteorological Imager(JAMI) 센서에서 제공되는 매시간 Full-disk 검정된 복사량 및 휘도온도를 알고리즘의 입력 자료로 사용하였다. 5개 JAMI 채널의 중심 파장은 0.725 ㎛(VIS), 10.8 ㎛(IR1), 12.0 ㎛(IR2), 6.75 ㎛(IR3), 3.75㎛(IR4)에 위치해 있다.

구름 정보 산출물의 검증을 위해 구름화소를 청천화소로부터 가려내는 전처리 과정이 필요하다. 현업에서는 CMDPS 알고리즘에서 구름탐지 알고리즘이 이 역할을 담당하나, 본 알고리즘의 검증은 간소화된 ISCCP 구름탐지 기법(Rossow and Garder 1993a)을 활용하였다. ISCCP는 구름탐지를 위해, 다음과 같은 VIS과 IR채널의 스펙트럴 시험을 사용한다.

$$\text{Clear: } (BT_{IR1}^{clr} - BT_{IR1}) \leq IRTHR \text{ and } (L_{VIS} - L_{VIS}^{clr}) \leq VISTHR$$
$$\text{Cloudy: } (BT_{IR1}^{clr} - BT_{IR1}) > IRTHR \text{ or } (L_{VIS} - L_{VIS}^{clr}) > VISTHR \qquad (2)$$

여기서 BT_{IR1}^{clr}, BT_{IR1}, L_{VIS}, L_{VIS}^{clr} 는 각각 IR1 전천 휘도온도, IR1 청천 휘도온도, VIS 전천 복사량, VIS 청천 복사량이다. L_{VIS}는 ISCCP 알고리즘과 같이 퍼센트 비율로 조정된 복사량이다. 경계값 IRTHR은 12.0 K이며 VISTHR은 육지에 대하여 6.0 %, 해양에 대하여 3.0 %이다. 여기서 구름탐지의 유효성은 주로 청천 복사량의 정확도에 의해 결정이 됨을 유념해야 할 것이다(Rossow and Garder 1993b). 본 검증에서는 BT_{IR1}^{clr}(L_{VIS}^{clr})를 2006년 8월 한 달간 각 UTC에 대한 최대(최소)값으로 설정하였다. VISTHR는 ISCCP의 값과 동일하지만, 높게 계산된 IR 청천 휘도온도 때문에 IRTHR은 Rossow and Gardar (1993a)에서 제시한 값보다 육지에 대해 6 K, 해양에 대해 1 K가 높다. 따라서 ISCCP 알고리즘보다 구름화소 선별이 더욱 엄격하다. 밤에는 식 (2)에서 IR1 조건만을 이용한다.

위 방법에 의해 탐지된 운량은 JAMI FOV에서 2006년 8월 평균 약 57.3 %를 차지한다. 이 값은 다른 전구 운량 기후값의 추정 결과와 비교할만하다. Rossow et al.(1993)에 의하면 ISCCP C2(1984-1988)에서 62.7 %, Gridded surface weather station reports(SOBS)(1971-1981)에서 61.2 %, METEOR(1976-1988)에서 61.4 %, Nimbus-7(1980-1984)에서 51.8 %로 추정하였다. 주목하여야 할 점은 Moderate Resolution Imaging Spectroradiometer(MODIS)의 운량은 검증기간 평균 77.6 %로, JAMI의 운량보다 훨씬 많다는 것이다. 이것은 MODIS가 18개의 밴드를 가지고 더 좁은 FOV에서, 엷은 권운을 포함한 다양한 형태의 구름을 탐지하기 때문이다. 따라서 위 방법에 의한 구름탐지 결과는 실제에 비해 상당한 불확실성을 내포하고 있을 것이다. 이를 이용한 구름 정보 산출물 또한 불확실성을 가지고 있음은 자명하다. 그러나 위 간소화된 구름탐지 방법에 의해 간과된 엷은 구름이 구름광학두께와 유효입자반경에는 상대적으로 적은 영향을 끼칠 것으로 생각된다.

3.4.1.2. 검증방법설명

검증은 2006년 8월 한 달간 JAMI Full-disk 영상에 대해 수행되었다. 이 기간은 제한된 계산 공간을 감안하여 결정되었지만, 이기간의 FOV는 사실 정지궤도 위성 탐지에 영향을 주는 지표면, 운형, 대기의 가스 연직분포, 관측 및 태양각이 가질 수 있는 모든 상황을

포함한다. 게다가, 이 기간 동안 Saomi와 Bopha와 같은 주요 태풍이 활동하여 한반도 및 일본에 상륙하였다. 통신해양기상위성 활용의 주목적이 악기상 예보임을 감안할 때, 이 검증 기간은 알고리즘의 수행 능력을 시험할 수 있는 최적의 기간이다.

본 검증에서는 두 가지 형태의 구름 산출물, 즉 전통적인 알고리즘을 통해 산출된 "기본 산출물(base product)"과 서울대학교 허창회 교수팀이 독자 개발한 현재 버전 알고리즘(Choi et al. 2007)의 "최종 산출물(final product)"을 각각 검증/비교하여 현재 버전 알고리즘의 향상 점을 파악하였다. 기본 구름광학두께 및 유효입자반경은 decoupling method(Choi et al. 2007)를 사용하지 않고 산출되었으며, 최종 구름광학두께 및 유효입자반경은 decoupling method를 사용하여 산출되었다. 마지막으로 기본 운정고도는 IR1채널의 복사휘도만을 이용하여 산출, 본 검증에서 사용한 각 산출물의 명칭은 Table 1에 요약되어 있다.

Table 3. Definitions of terms used in this analysis.

Term	Unit	Definition
Base COT/ER	unitless/m	Cloud optical thickness and effective radius are roughly retrieved by using measured VIS and IR4 radiances that remain to include both thermal and reflected components.
Final COT/ER	unitless/m	Cloud optical thickness and effective radius are retrieved by the sun reflection method that uses the decoupled radiances, i.e. cloud-reflected components.

위에서 정의된 기본, 최종, 그리고 MODIS 산출물을 4가지 절차로 비교하였다. 4가지 결과 모두 알고리즘을 최적의 상태로 보정하고, 산출물의 취약점을 파악하기 위한 유용한 자료를 제공한다.

(1) 장면분석

장면분석은 본 검증의 첫 번째 활동이다. 장면분석은 복사량과 산출물 영상간의 비교를 의미하며, 이 활동을 통해 산출물의 전체적인 신뢰성을 개략적으로 검토할 수 있다.

(2) 기후값 비교

기후값 비교는 산출물이 기후자료로서 신뢰할만한 자료인지 확인하는 활동이다. 또한 산출값이 어떻게 편중(bias)되어 있는지 파악할 수 있다. 오랜 기간의 자료가 확보되어야 하나, 본 검증에서는 2006년 8월의 평균값으로 한정되었다. 기후값은 다양한 조건에 대해 나누어 비교해야 산출값 편중의 원인을 파악할 수 있다. 예를 들어 주간, 야간, 액체상 구름, 얼음상 구름, 남반구, 북반구, 극지방, 열대지방, 중위도지방 등에 대해 MODIS 산출물의 기후값과 비교한다.

(3) 시계열 비교

시계열 비교는 관심지역에 대해 검증기간 기간 동안의 일변화를 검증보조 자료와 비교하는 활동이다. 관심지역은 육지, 해양, 사막, 눈/얼음과 같은 다양한 지표면 조건과, 저·중·고위도에서 골고루 선택된다. 본 검증에서 선택된 관심지역은 9개 지역으로 서울, 중국 화북평야, 고비사막, 티벳고원, 남지나해, 필리핀해, 동태평양, 베링해, 남극지역이다.

(4) 화소 비교

마지막으로 구름 정보 산출물을 화소단위로 보조 자료와 비교하여 에러 범위를 파악한다. 본 검증에서 MOD06 collection 5 구름 자료가 보조 자료로 사용되었다. 화소비교를 위한 검증 영역은 북서태평양(10° −30° N, 113° −149° E)으로 한정하였다. 이 지역의 많은 열대 저기압성 소용돌이들은 강한 바람과 나선형의 강수대를 갖는 잘 발달된 대류활동으로 다양한 운형이 관측된다(Kim et al. 2006). MODIS와 JAMI 영상 사이의 시공간적 불일치를 피하기 위해, 바람의 경로를 고려해 두 영상 간 50 km 거리와 30분이내의 최적 화소를 상호 비교하였다. 이 조건하에서 약 2,160,000 구름 화소쌍이 검증에 사용되었다(구름광학두께의 경우 이의 절반). JAMI의 영상 화소는 4 km 해상도이나, MODIS MOD06 구름광학두께와 유효입자반경은 1 km 해상도이다. 두 영상 화소 간 해상도 차이는 본 화소 비교 결과의 불확실성을 유발할 수 있다.

3.4.2. 검증자료

(1) CMDPS 검증 (COLL/VAM)

CMDPS 구름광학두께를 검증하기 위해서 사용된 자료는 MODIS Terra와 Aqua의 11월 1일부터 5일까지 자료를 사용하여 검증을 하였다. 다른 구름 분석 자료와 동일하게 위도별로 분리하여 (적도: 위도 30도 미만, 중위도: 남북30−60도) 통계값을 계산하도록 하였다. 또한 두꺼운 구름광학두께, 큰 태양천정각에서는 부정확도가 커지므로 구름광학두께가 16보다 클 경우와 작을 경우, 그리고 태양천정각에 따라 통계값을 산출하도록 하였다. 이외에도 구름상과 유효입자반경에 따라서도 각각 검증을 하였다.

(2) 개발자 자체 검증

검증에 사용된 JAMI 복사량 및 관측각의 공간 해상도는 4 km이다. Full−disk 영상은 동아시아 및 서태평양, 호주, 남극의 일부분(80.5° S−80.5° N, 60.4° E−139.4° W)을 포함하는데 통신해양기상위성의 위치와 유사하다.

JAMI 영상을 이용해 산출된 산출물과 비교하기 위해 MODIS 구름 자료(MOD06, collection 5)를 사용하였다. 이 자료에는 1 km 천저(nadir) 해상도의 구름광학두께와 유효입자반경이 포함되어 있다(Platnick et al. 2003). 이전 버전보다 collection 5 자료에서

향상된 점은 다른 문헌에서 찾을 수 있다(Baum et al. 2005, King et al. 2006, Yang et al. 2007). 본 검증에서는 2006년 8월 5-11일 기간 북서태평양(10° -30° N, 113° -149° E)에서의 그래뉼(granule; 5분 관측 자료)을 수집하였다.

MOD06의 구름광학두께 및 유효입자반경은 가시채널과 근적외채널(0.6, 0.8, 1.2, 2.1 ㎛)을 동시에 사용하여 결정된 대기 기둥 전체를 대표하는 값이다. MOD06 구름광학두께의 최소 산출 범위는 0.1(Choi et al. 2005)이며 최대 산출 범위는 100까지이다. 유효입자반경의 경우 유효한 산출범위는 액상 구름의 경우 2~30㎛, 얼음상 구름의 경우 5~90㎛이다. 두 산출물 모두 소수점 둘째자리까지 산출된다. MODIS 자료와 비교하기 위해 본 CMDPS 산출물도 동일한 범위 내에서 산출되었다.

MODIS 격자화 된 level-3 일별 대기 자료(MOD08, collection 5)도 동일한 검증기간에 대해 수집되었다. MOD08은 1° 격자의 값을 가지며 MOD06으로부터 계산된다. MOD08은 검증기간동안 구름 산출정보의 평균값이나, 주어진 격자에 대한 시계열 분석을 위해 별도로 사용되었다.

3.4.3. 시공간일치방법

(1) CMDPS 검증 (COLL/VAM)

다른 구름분석 알고리즘의 검증과 동일한 방법으로 -8분~30분 내 범위의 자료를 사용하여 시공간을 일치시켰다. 먼저 고위도 (남북60° 이상)는 검증에서 제외하였다. 시공간의 일치를 위해서는 homogeneous한 경우에 대해서만 검증을 하기 위해 MODIS의 5×5화소에서 1-표준편차 (1-standard deviation)이상의 차이가 나는 부분은 검증에서 제외하였다.

(2) 개발자 자체 검증

화소 비교 시 CMDPS CLA 기준, 50 km, 30분 이내에 들어오는 화소를 평균하여 시공간을 일치시켰다.

3.4.4. 검증결과분석

(1) CMDPS 검증 (COLL/VAM)

Table 4. Validation results of COT

	Reference	Time	Region	R	Bias	RMSE
COT	MOD	11/1~11/5	Global	0.73	2.16	3.32
			Low	0.73	1.98	3.05
			Mid	0.68	2.79	3.97
			COT < 16	0.62	2.18	2.84
			COT > 16	0.84	-0.23	19.04
			SOA <30	0.73	2.05	3.36
			SOA >30	0.65	2.27	3.18
			Water	0.54	2.02	2.85
			Ice	0.82	2.77	4.61
	MYD	11/1~11/5	Global	0.90	1.71	3.57
			Low	0.93	1.63	3.79
			Mid	0.66	1.92	2.85
			COT < 16	0.58	1.86	2.57
			COT > 16	0.79	-21.90	31.57
			SOA <30	0.76	1.43	4.35
			SOA >30	0.83	1.84	2.99
			Water	0.52	1.61	2.45
			Ice	0.96	2.12	6.18

Table 4는 2008년 11월 1일부터 5일까지 검증 결과 보여주고 있다. 앞에서 언급한 것처럼 다양한 검증 조건에 따른 MODIS와 CMDPS 구름광학두께의 상관계수, Bias, 그리고 RMSE의 통계치를 보여주고 있다.

(2) 개발자 자체 검증

1) 장면분석

Fig. 6은 2006년 8월 7일 0333 UTC JAMI 복사량 영상의 예시이다. 구름은 Intertropical convergence zone(ITCZ)를 따라 분명하게 보인다. VIS 영상에서 태양빛의 산란으로 인해 광학적으로 두꺼운 구름은 밝게 보인다. 해양과 같은 어두운 지표면에 비해 구름이 잘 구별된다. IR 영상에서 밝은 색은 상대적으로 낮은 값에 해당하며, 고도가 높은 구름이 구름꼭대기로부터 더 낮은 IR 복사량을 방출하기 때문에 밝게 보인다. IR3 영상에서는 오직 400 hPa 이상의 높은 구름만이 밝게 보인다. 이는 중하층 대류권에서 강력한 수증기 흡수가 일어나기 때문이다. 그러나 IR1이나 IR2와 같은 적외창 채널에서는 낮은 구름이 뚜렷이 판명된다. IR4 복사량은 일반적으로 작은 구름입자, 액체상 입자에 대해 높은 값을 가진다.

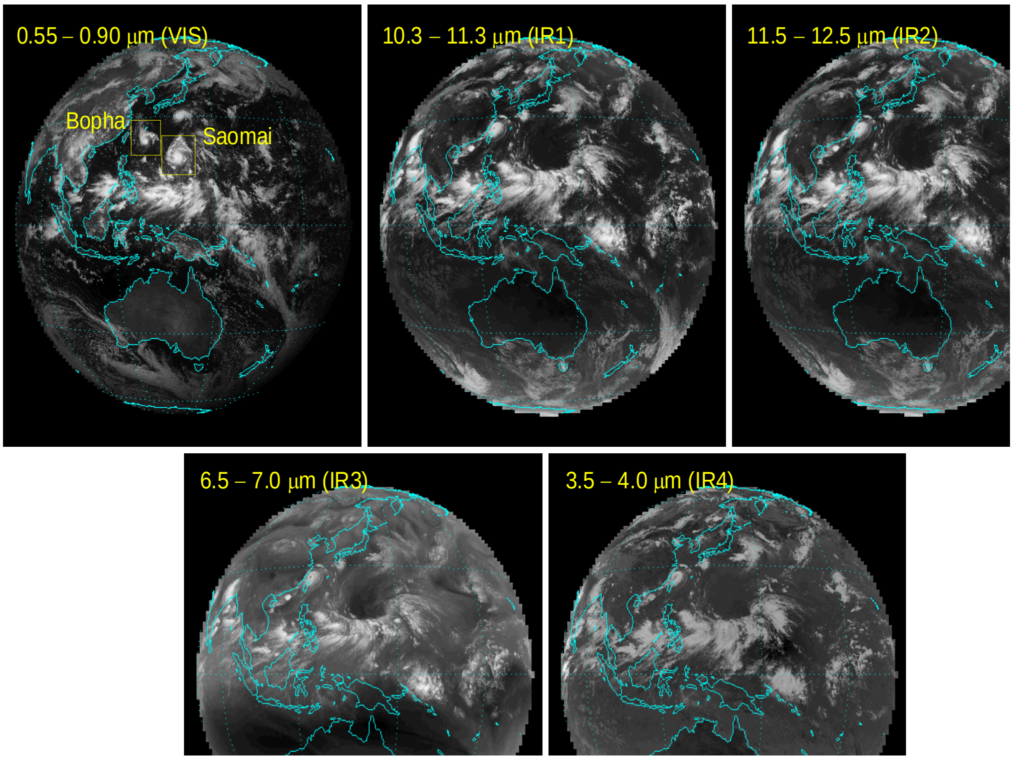

Fig. 6. JAMI/MTSAT-1R radiance imagery for the five spectral channels centered at 0.725 (VIS), 10.8 (IR1), 12.0 (IR2), 6.75 (IR3), and 3.75 m (IR4) for 0333 UTC August 7, 2006. Except for the VISchannel, the brighter color corresponds to a relatively low value in W m2 sr1 m1. The full-disk imagery covers East Asia, West Pacific, Australia, and a part of the Antarctic region (80.5S80.5N, 60.4E139.4W).

위에서 논의한 5개 영상의 스펙트럴 성질을 감안할 때, 이 시각 영상은 유추되는 구름성질에 따라 크게 세 가지의 영역으로 특징 지워진다.

(i) 열대 서태평양에서 태풍의 구름을 포함하여 매우 높고 광학적으로 두꺼운 구름
(ii) 동태평양의 높고 엷은 구름
(iii) 넓게 분포한 낮고 엷은 구름과 호주의 남서쪽 바다위의 높고 두꺼운 구름

(i)는 높은 VIS, 낮은 IR1, 낮은 IR2 복사량으로 유추, (ii)는 낮은 VIS, 낮은 IR1, 낮은 IR2 복사량으로 유추, (iii)는 넓게 분포한 낮은 VIS, 높은 IR1, 높은 IR2 복사량 및 나뭇가지 모양의 높은 VIS, 낮은 IR3 복사량으로 유추된다. 이 세 가지 유추된 구름의 특징을 CMDPS 알고리즘 산출물과 비교한다. 여기서 모든 구름 정보 산출물을 종합적으로 검토하여야 한다.

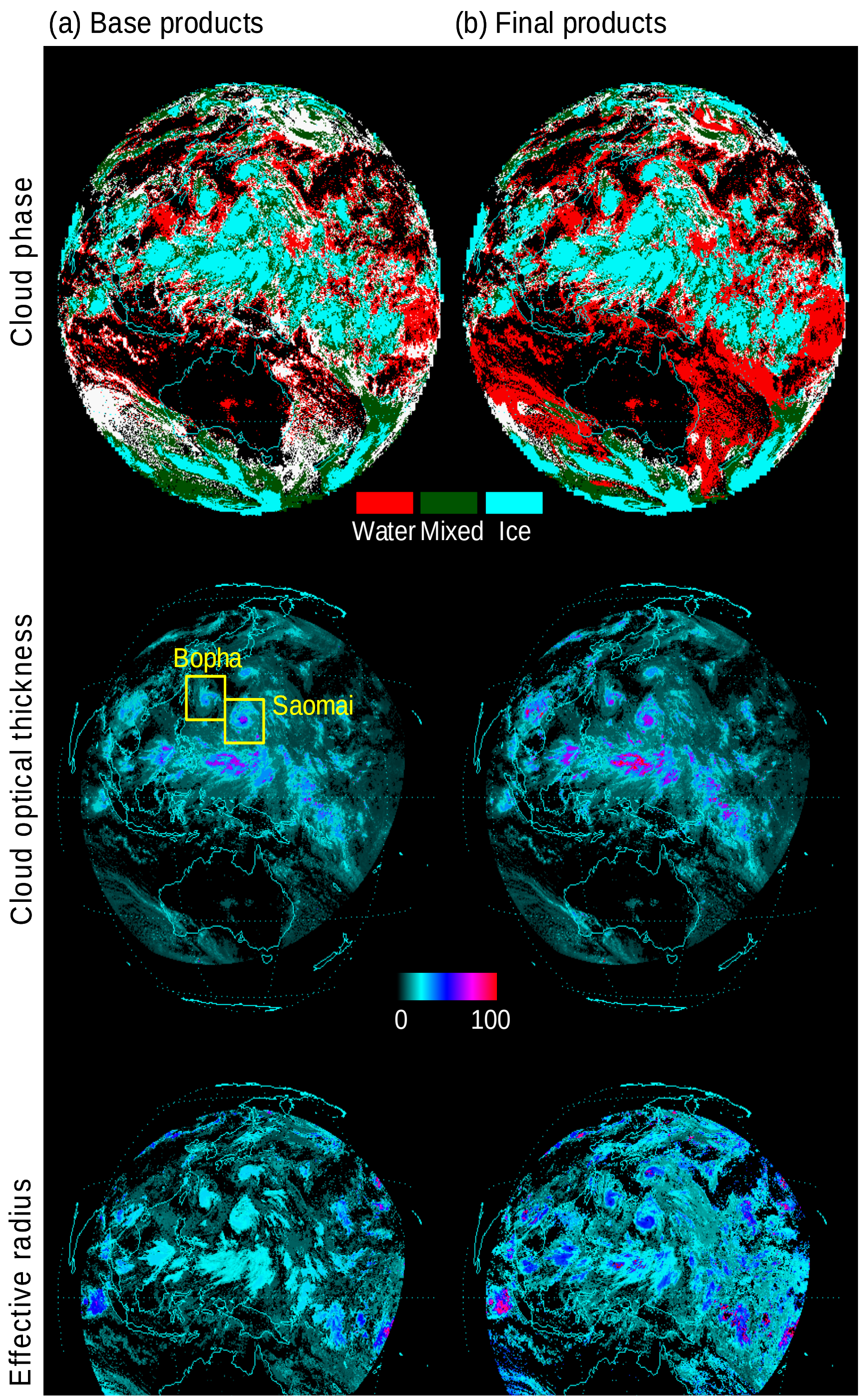

Fig. 7. Cloud optical thickness and effective radius derived by the CLA from the JAMI level−1b calibrated radiances shown in Figure 1. Base products (left) are the results of conventional methods or without correction methods, and final products (right) from improved methods or with the correction methods developed in the present study.

Fig. 7은 구름광학두께, 유효입자반경의 기본 산출물(좌)과 최종산출물(우)이다. 전체적으로 두 산출물간 차이가 분명하다. 최종 산출물이 기본 산출물에 비해 위에서 언급한 세 가지 주요 구름 특징을 더 잘 나타낸다. 최종 구름광학두께(유효입자반경)는 ITCZ와 태풍에서 기본 산출물에 비해 더 큰 값을 갖는다. 매우 높고 두꺼운 구름이 열대 서태평양에서 최종 산출물들에서 더 뚜렷하다. 60도 이상의 높은 관측각에 대해서 구름광학두께를 추정할 수 없지만, 최종 구름광학두께는 동태평양의 높고 엷은 구름과 호주근처의 높고 두꺼운 구름의 특징을 잘 포착하고 있음을 알 수 있다.

2) 기후값 비교

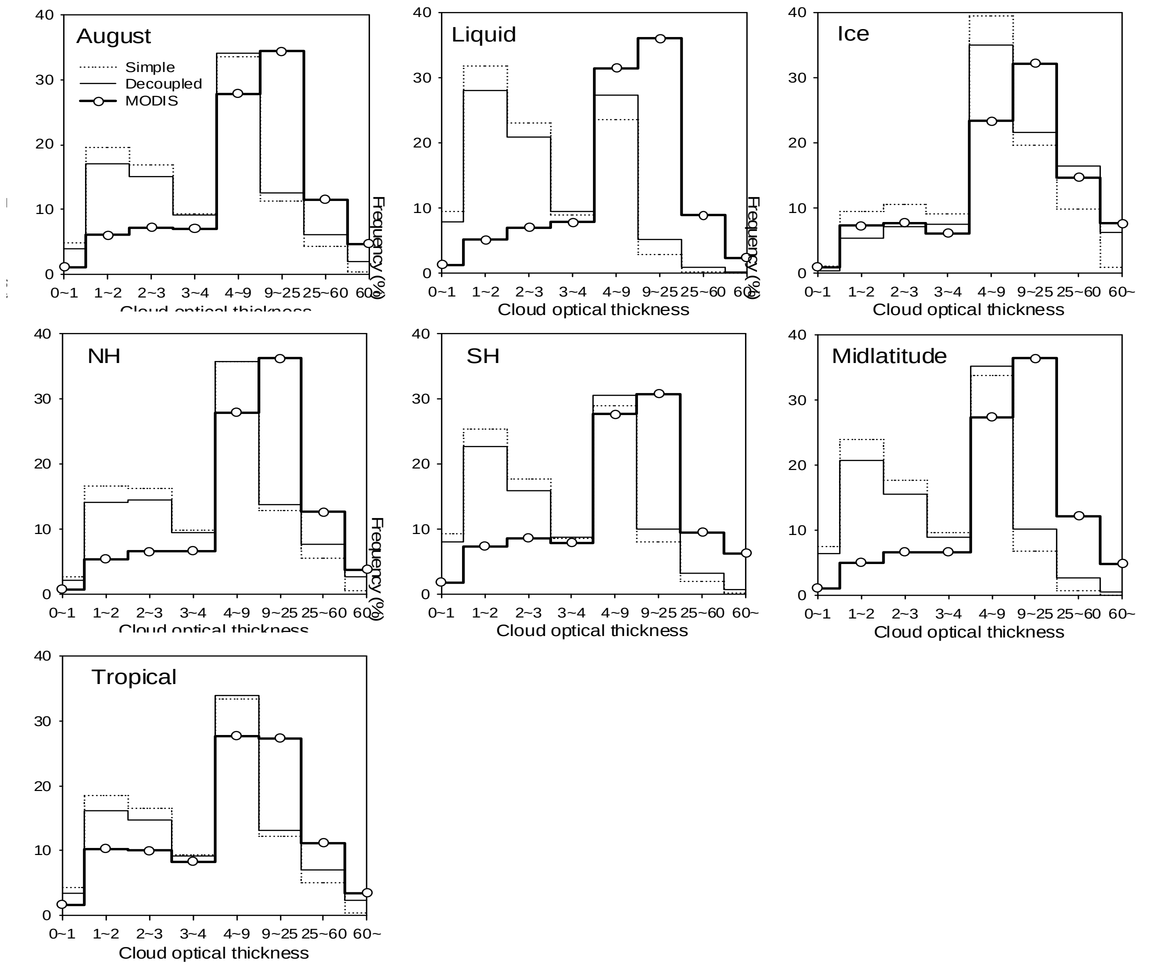

Fig. 8. Relative frequency (in %) of cloud optical thickness without using the decoupling method (i.e., base products), using the decoupling method (i.e., final products), and MODIS data to the total clouds for the corresponding conditions. SH and NH stand for the Northern and Southern Hemispheres, respectively.

다양한 조건하에서 구름광학두께의 한 달 기후값의 상대 빈도를 보았다(fig. 8). 가로축의 간격은 ISCCP 운형 분류를 위한 구름광학두께의 기준에 기초한 값이다(Rossow and Schiffer 1999). 점선, 실선, 굵은 선은 각각 기본, 최종, MODIS 산출물을 의미한다. 산출된 구름광학두께는 일반적으로 MODIS 보다 과소 추정된다. 최종 산출물 및 MODIS 산출물 모두 4-6, 9-25에서 높은 값을 갖는다. 구름광학두께가 4미만인 화소는 MODIS의 빈도가 더 적지만, 구름광학두께가 9-25사이인 화소의 빈도는 MODIS의 빈도가 모든 경우에 대하여 더 크다. 이러한 일관된 편중현상은 모델 계산으로부터 유발되었을 것이며, 조견표의 튜닝을 통해 최소화 될 수 있다.

MODIS와 우리 산출물간의 차이는 액체상과 얼음상의 반사도 차이에 의해서도 유발된다. Fig. 8에서, 그 차이는 얼음상보다 액체상일 때 더 크다. 액체 수적은 얼음 입자보다 더 효과적으로 태양빛을 반사시킨다. 결과적으로 액체상 구름으로부터 반사된 복사량은 같은 광학두께에 대해 얼음상 구름으로부터 반사된 복사량에 비해 더 크다. 이 때문에 구름 정보 산출 알고리즘은 얼음상 구름이 액체상 구름으로 잘못 판독된 경우 구름광학두께를 과소 추정할 수 있다. 이것을 달리 말해 구름상이 구름광학두께 산출 정확도에 매우 중요한 역할을 하고 있다.

유사한 분석을 유효입자반경에 대해서 실시하였다(fig. 9). 우리 산출물의 값이 MODIS 보다 약간 과소 추정되었다. 그러나 그 차이는 구름광학두께보다 작다. 유효입자반경은 두 산출물 모두 액체상에서 적으며 얼음상에서 크다. 액체상 입자는 2∽30㎛를, 얼음입자는 5∽64㎛를 갖는다. 액체상에서 10∽20㎛가 얼음상에서 20∽30㎛의 크기에 대해 가장 빈도수가 높다. 유효입자반경에서는 남북반구 간 차이가 적다. 열대지방에서 MODIS와의 차이가 크지만, 중위도 지방에서는 MODIS와의 차이가 거의 없다. 유효입자반경은 IR4의 복사량에 민감하기 때문에, 이러한 결과는 우리 알고리즘에서 관측된 IR4 복사량으로부터 열적성분과, 지표반사 성분을 분리해내는 기술(Choi et al. 2007)이 특히 중위도에서 탁월함을 알 수 있다.

지금까지 MODIS와 산출물을 비교해 보았다. 그러나 최종 알고리즘의 특징을 파악하기 위해 기본산출물과 최종산출물을 비교할 필요가 있다. Fig. 8에서 점선과 실선을 비교해보면 decoupling 방법을 통해 광학두께 4미만의 엷은 구름의 빈도는 감소하며, 그 대신 두꺼운 구름의 빈도는 증가한다. 또한 Fig. 9에서는 유효반경 10미만의 작은 입자를 가진 구름의 빈도는 감소하고 큰 입자를 가진 구름의 빈도는 증가한다. 구름광학두께가 1과 9사이인 구름은 열대 에너지 수지 균형에 매우 중요하다(Choi and Ho 2006). 따라서 이러한 종류의 구름이 decoupling 방법에 의해 변경되면 구름의 복사효과 추정도 변경이 되어야 한다. 최종산출물이 기본산출물에 비해 더 MODIS에 가까운 값을 갖기 때문에 decoupling 방법이 구름광학두께와 유효입자반경의 정확도 증가와 함께, 구름의 복사효과에 대한 이해를 증진시키는데 기여하는 것은 자명하다.

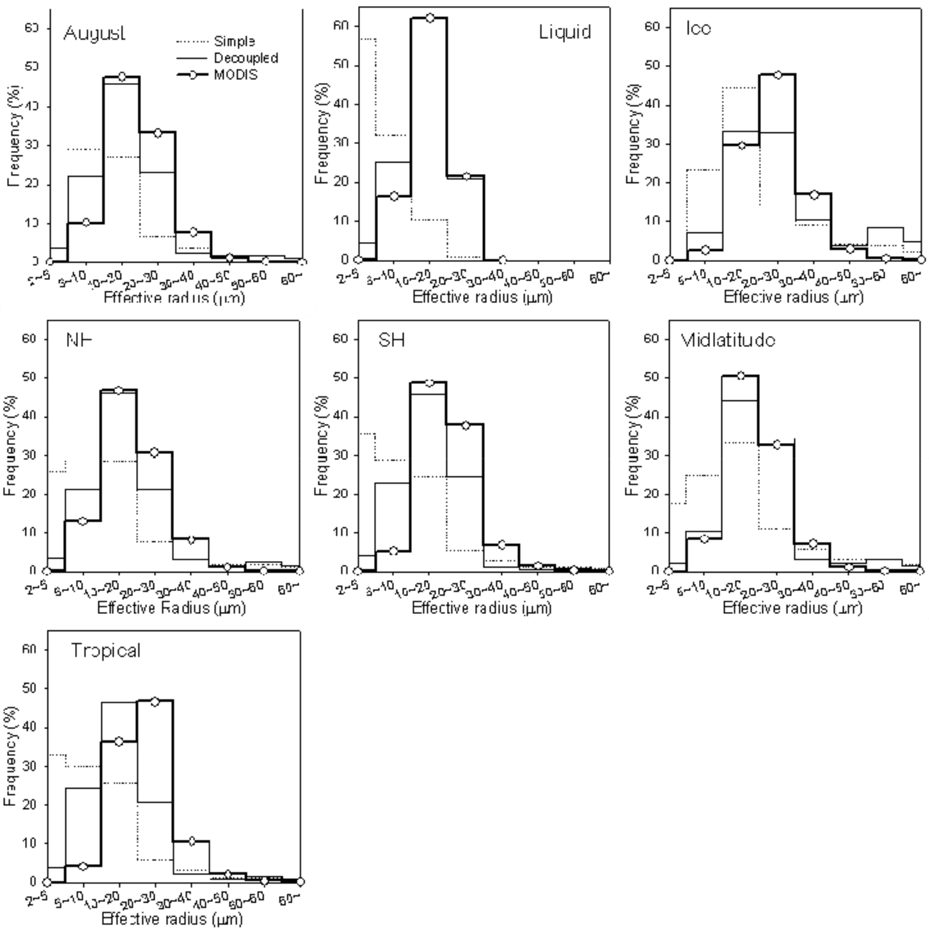

Fig. 9. Same as figure 8 but for cloud effective radius (in ㎛).

3) 시계열 비교

기후값 비교가 산출물의 검증에 매우 중요한 정보를 제공하긴 하나 MODIS 산출물과의 실제적 일치성을 보여주지는 못한다. 이장에서는 9개의 관심지역에 대해 산출물의 시계열을 분석하였다. MTSAT 산출물은 매시간 4 km의 해상도에서 산출되기 때문에 MOD08 격자화 된 MODIS 자료와의 비교를 위해 1° 격자에 대하여 매시 평균을 하였다. MODIS/Terra는 모든 지역에 대하여 아침 10시 30분경을 지난다. 따라서 매시간 MTSAT 자료가 MODIS의 자료와 시각이 정확히 일치하지는 않으며, 단지 매시 변동성과 유사한 일 변동성을 확인할 수 있다.

구름광학두께와 유효입자반경은 위성 천정각이 60° 미만 일 때 산출이 된다. 따라서 기본 산출물(a)와 최종산출물(b)은 단지 5개의 관심지역에서 주간에만 산출된다(figures 10과 11). 최종 산출물은 기본 산출물에 비해 MODIS 자료와 더 가깝다. 이러한 향상은 decoupling 방법 덕택인데 지역과 관계없다. 그러나 구름광학두께와 유효입자반경의 매시간 변동성이 매우 크다. 이것은 산출에 태양천정각의 영향 때문이다. 일출과 일몰에 가까울수록 에러가 높아질 것이다.

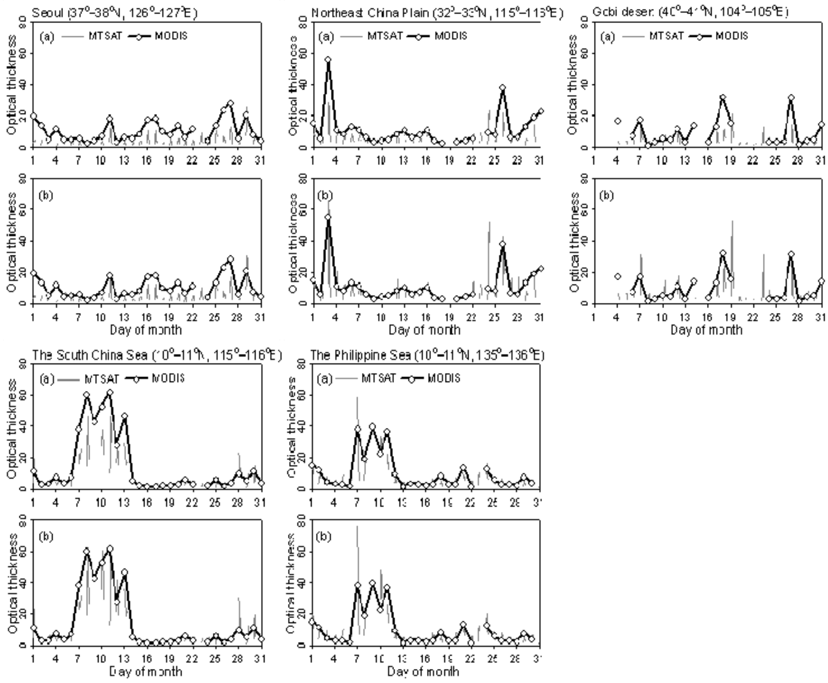

Fig. 10. Same as fig 8 but for base COT using the VIS and IR4 radiances (a), and final COT corrected using the decoupling method in order to have a reflected component from clouds only in the radiances (b).

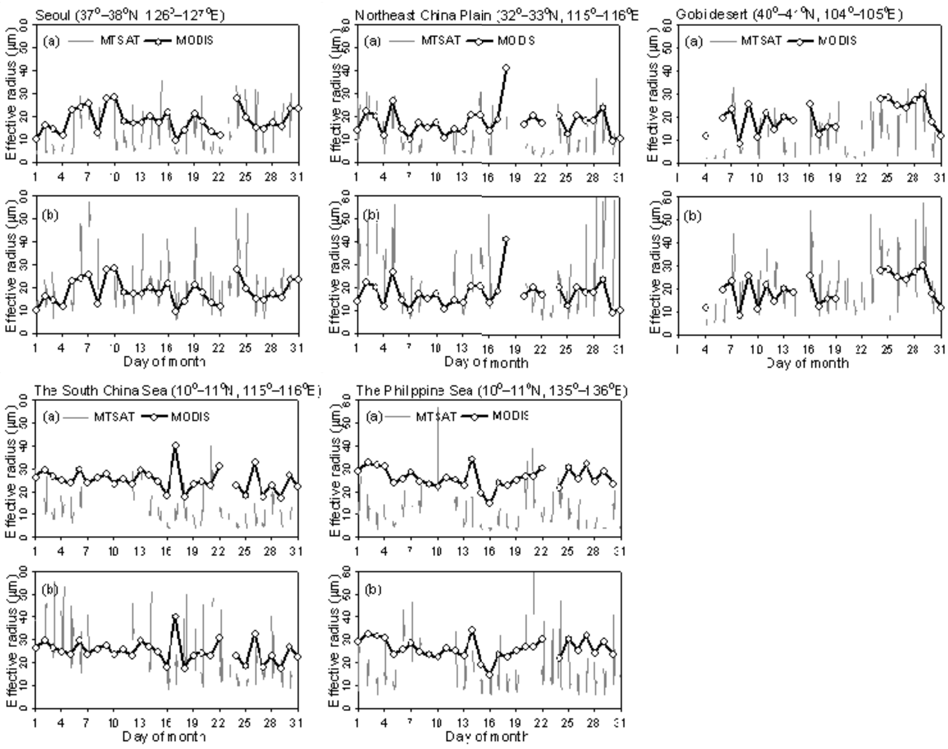

Fig. 11. Same as fig 9 but for base ER (a) and final ER (b).

4) 화소 비교

Fig. 12는 MTSAT과 MODIS 구름정보의 화소 비교 결과를 보여준다. 두 산출물간 차이의 최대값에 대한 상대 도수, 그리고 MODIS 자료 값에 대한 에러를 도식하였다. 에러는 MTSAT과 MODIS의 차이와 MODIS 산출물간의 비율로 표현되었다.

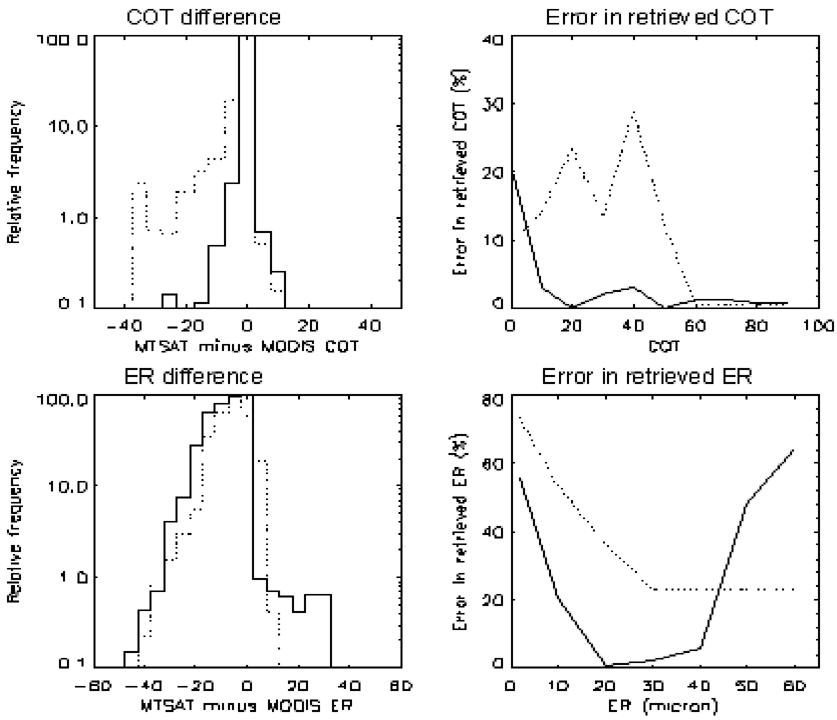

Fig. 12. Relative frequency of MTSAT minus MODIS COT/ER for the maximum values. Errors in the retrieved COT/ER (in %) with respect to the corresponding parameters. The solid and dotted lines indicate values from the final (corrected) and base (uncorrected) products, respectively.

최종 구름광학두께와 MODIS 산출물은 거의 ±5 이내에서 일치한다. 단지 약간의 화소(전체의 2 %)만이 MODIS 구름광학두께와 불일치하는데, 이 에러는 기본 구름광학두께에 비해 현격히 감소된 양이다. 기본 및 최종 구름광학두께 모두 광학적으로 매우 두꺼운 구름(광학두께 60이상)에 대해 매우 작다. 이것은 Choi et al. (2007)에서 물리적인 이유로 광학두께가 두꺼운 구름에 대해 더 많은 에러를 갖고 있다고 밝힌 것과 상반된다. 좀 더 세밀한 분석에 의하면 매우 두꺼운 구름의 발생은 자연 상태에서 매우 드물게 발생하므로, 시공간 불일치에 따른 에러가 항상 내재되어 있는데 화소 비교 과정에서 우연히 낮은 에러를 보일 수 있다.

구름광학두께와는 달리 최종 유효입자 반경은 MODIS의 값에 비해 큰 차이를 보인다. 이 불일치는 상당량의 화소에 대해 나타나는데 아마도 큰 입자(입자반경 40 ㎛이상)로부터 유발된 듯하다. 큰 입자에 대해 IR4 복사량이 덜 민감하므로 추정 정확도는 떨어지게 마련

이다. MTSAT으로부터 산출된 신뢰도 있는 유효입자 반경은 40㎛ 미만으로 볼 수 있다.

4. 산출결과 해석방법

VIS0.65㎛와 SWIR3.75㎛의 반사도는 백분율로 표시되며 0~100 %의 범위를 갖는다. 조견표는 지면알베도)의 조건하에 복사전달모델 “Santa Barbara DISORT Atmospheric Radiative Transfer (SBDART)"를 이용하여 계산한 결과이다. 또한 지표정보와 장면분석 결과가 입력 자료에 들어간다. 이를 이용하여 구름광학두께와 유효입자반경을 산출한다. 구름광학두께의 값은 0~64의 범위를 가지며 Prec.와 Acc.는 1이다.

Table 3. Detailed Output data for the COT algorithm.

OUTPUT DATA								
Parameter	Mnemonic	Units	Min	Max	Prec	Acc	Res	To
Cloud Optical thickness	cld_opt	-	0	128	1	1	pixel	COT
Effective Cloud Radius	eff_cld_rad	-	0	64	1	1	pixel	ER

5. 천리안 발사 후 COMS화 및 알고리즘 개선

프로그램 내의 코드 에러로 인하여 육지 부근에서 매우 큰 COT값이 산출되어 육지해상 불연속이 발생하여 아래와 같이 코드를 수정하였다. COT가 이용하는 LUT값은 R = 0인 경우와 R = 0.5인 경우에 대해 구성되어있다. COT 알고리즘은 R = 0와 R = 1인 경우의 복사량 차이를 필요로 하므로 scaling을 위해 2를 곱해서 사용한다(CMDPS 최종보고서, Fig. 2.12.32). 그러나 실제 코드 상에서는 2를 곱하는 대신에 제곱을 함으로서 육지 부분에서 매우 큰 값을 가지게 되어 불연속이 발생 하였다(Fig. 13).

```
!-------------------------------------------------------------------------
! Radiance decoupling
!-------------------------------------------------------------------------
! Remove thermal component at 3.7um

!            cla_rad_swir(i,j) = a*((radiance(i,j)%ir1)**2) + b*radiance(i,j)%ir1 + c
           cla_rad_swir(i,j) = a * (radiance(i,j)%ir1*radiance(i,j)%ir1) + &
                               b * radiance(i,j)%ir1 + c

           cla_rad_swir_tmp(i,j) = radiance(i,j)%swir - cla_rad_swir(i,j)

           cla_rad_vis_tmp(i,j) = radiance(i,j)%vis

!            vissr(:)  = albedo(i,j)*(lut2(:)-lut0(:))*2
!            swirsr(:) = albedo(i,j)*(lut3(:)-lut1(:))*2
           vissr (:) = albedo(i,j)*(lut2(:)-lut0(:))*(lut2(:)-lut0(:))
           swirsr(:) = albedo(i,j)*(lut3(:)-lut1(:))*(lut3(:)-lut1(:))
```

Fig. 13. Modified COT code for removing land-sea discontinuities

코드를 수정하여, 수정후 불연속이 해소되었으며 그 결과는 Fig. 14와 같다. 육상에서 나타나던 큰 값들이 제거되고 대신에 해상의 값과 불연속 없이 COT 값이 잘 산출된 것을 볼 수 있다.

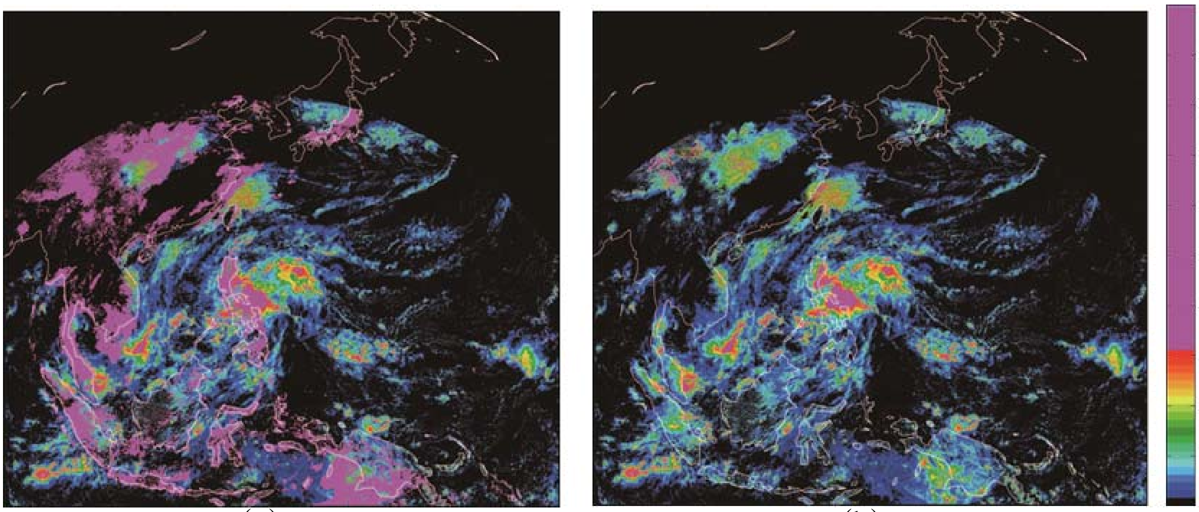

(a) (b)

Fig. 14. Cloud optical thickness (a)before and (b)after correcting program code at 15th, Nov, 2011.

6. 문제점 및 개선 가능성

표준화코드에 품질검사 코드 (Table 4)의 삽입, 돌발 상황 대비(Contingency plan) 코드의 삽입 등이 향후 개선과제로 남아 있다.

Table 4. Quality test result for the COT algorithm.

Quality test result			
Parameter	bit	Value	Meaning
cloud optical thickness	5	from 0 up to 64; step: 1	undefined
effective cloud radius	5	from 0 up to 32; step: 1	undefined
describe COMS input data	2	0	undefined
		1	all useful COMS channel available
		2	at least one useful COMS channel available
define illumination and viewing conditions	3	0	undefined
		1	night
		2	twilight
		3	day
		4	sunglint
describe the quality of the processing itself	2	0	non processed
		1	good quality
		2	poor quality
		3	bad quality

7. 참고문헌

Baum, B.A., Yang, P., Heymsfield, A.J., Platnick, S., King, M.D., Hu, Y.X. and Bedka, S.T., 2005, Bulk scattering properties for the remote sensing of ice clouds. Part II: Narrowband models. Journal of Applied Meteorology, 44, pp. 1896-1911.

Choi, Y.-S., Ho, C.-H. and Sui, C.-H., 2005, Different optical properties of high cloud in GMS and MODIS observations. Geophysical Research Letters, 32, L23823, doi:10.1029/2005GL024616.

Choi, Y.-S. and Ho., C.-H., 2006, Radiative effect of cirrus with different optical properties over the tropics in MODIS and CERES observations. Geophysical Research Letters, 33, L21811, doi:10.1029/2006GL027403.

Choi, Y.-S., Ho, C.-H., Ahn, M.-H. and Kim, Y.-M., 2007, An exploratory study of cloud remote sensing capabilities of the Communication, Ocean and

Meteorological Satellite (COMS) Imagery. International Journal of Remote Sensing, 28, pp. 4715−4732.

Kim, J.−H., Ho, C.−H., Lee, M.−H., Jeong, J.−H. and Chen, D., 2006, Large increase in heavy rainfall associated with tropical cyclone landfalls in Korea after the late 1970s. Geophysical Research Letters, 33, L18706, doi:10.1029/2006GL027430.

King, M.D., Tsay, S.C., Platnick, S.E., Wang, M. and Liou, K.N., 1997, Cloud retrieval algorithms for MODIS: optical thickness, effective particle radius, and thermodynamic phase. In MODIS Algorithm Theoretical Basis Document (NASA).

King, M.D., Platnick, Hubanks, P.A., Arnold, G.T., Moody, E.G., Wind, G., and Wind, B., 2006, Collection 005 Change Summary for the MODIS Cloud Optical Property (06_OD) Algorithm. Available online at: modis−atmos.gsfc.nasa.gov/C005_Changes/C005_CloudOpticalProperties_ver311.pdf.

Liou, K.N., 2002, An introduction to atmospheric radiation 2nd ed.. Academic Press, San Diego.

Menzel, W.P., Smith, W.L. and Stewart, T.R., 1983, Improved cloud motion wind vector and altitude assignment using VAS. Journal of Climate and Applied Meteorology, 22, pp. 377-384.

Menzel, W.P., Frey, R.A., Baum, B.A. and Zhang, H., 2006, Cloud top properties and cloud phase algorithm theoretical basis document, In MODIS Algorithm Theoretical Basis Document, NASA.

Nakajima, T.Y. and King, M.D., 1990, Determination of the optical thickness and effective particle radius of clouds from reflected solar radiation measurements, Part 1: Theory. Journal of the Atmospheric Sciences, 47, pp1878−1893.

Nakajima, T.Y. and Nakajima, T., 1995, Wide−area determination of cloud microphysical properties from NOAA AVHRR measurement for FIRE and ASTEX region. Journal of the Atmospheric Sciences, 52, pp. 4043−4059.

Platnick, S., King, M.D., Ackermann, S.A., Menzel, W.P., Baum, B.A., Riedi, J.C. and Frey, R.A., 2003, The MODIS cloud products: Algorithms and examples from Terra. IEEE Transactions on Geoscience and Remote Sensing, 41, pp. 456−473.

Rossow, W.B. and Garder, L.C., 1993a, Cloud detection using satellite measurements of infrared and visible radiances for ISCCP. Journal of Climate, 6, pp. 2341−2369.

____ and ____, 1993b, Validation of ISCCP cloud detections. Journal of Climate, 6, pp. 2370−2393.

____, Walker, A.W. and Garder, L.C., 1993, Comparison of ISCCP and other cloud amounts. Journal of Climate, 6, pp. 2394−2418.

____ and Schiffer, R.A., 1999, Advances in understanding clouds from ISCCP. Bulletin of the American Meteorological Society, 80, pp. 2261-2287.

Shupe, M.D., Matrosov, S.Y. and Uttal, T., 2006, Arctic mixed−phase cloud properties derived from surface−based sensors at SHEBA. Journal of the Atmospheric Sciences, 63, pp. 697711.

Strabala, K.I., Ackerman, S.A. and Menzel, W.P., 1994, Cloud properties inferred from 8-12−μm data. Journal of Applied Meteorology, 33, pp. 212-229.

Yang, P., Zhang, L., Hong, G., Nasiri, S.L., Baum, B.A., Huang, H.L., King, M.D. and Platnick, S., 2007,Differences between collection 4 and 5 MODIS ice cloud optical/microphysical products and their impact on radiative forcing simulations. IEEE Transanctions on Geoscience and Remote Sensing, 45, pp.2886-2899.

Verlinde, J. and Coauthors, 2007, The mixed−phase arctic cloud experiment. Bulletin of the American Meteorological Society, 88, pp. 205221.

Appendix

International Journal of Remote Sensing
Vol. 28, No. 21, 10 November 2007, 4715–4732

Taylor & Francis
Taylor & Francis Group

An exploratory study of cloud remote sensing capabilities of the Communication, Ocean and Meteorological Satellite (COMS) imagery

Y.-S. CHOI†, C.-H. HO*†, M.-H. AHN‡ and Y.-M. KIM†

†Climate Physics Laboratory, School of Earth and Environmental Sciences, Seoul National University, Seoul 151–742 Korea

‡Meteorological Research Institute, Korea Meteorological Administration, Seoul, Korea

(*Received 8 February 2006; in final form 24 January 2007*)

The present study documents optimal methods for the retrieval of cloud properties using five channels (0.6, 3.7, 6.7, 10.8 and 12.0 μm) that are used in many geostationary meteorological satellite observations. Those channels are also to be adopted for the Communication, Ocean and Meteorological Satellite (COMS) scheduled to be launched in 2008. The cloud properties focused on are cloud thermodynamic phase, cloud optical thickness, effective particle radius and cloud-top properties with specific uncertainties. Discrete ordinate radiative transfer models are simulated to build up the retrieval algorithm. The cloud observations derived from the Moderate-resolution Imaging Spectroradiometer (MODIS) are compared with the results to assess the validity of the algorithm. The preliminary validation indicates that the additional use of a band at 6.7 μm would be better in discriminating the cloud ice phase. Cloud optical thickness and effective particle radius can also be produced up to, respectively, 64 and 32 μm by functionally eliminating both ground-reflected and cloud- and ground-thermal radiation components at 0.6 and 3.7 μm. Cloud-top temperature (pressure) in ±3 K (±50 hPa) uncertainties can be estimated by a simple 10.8-μm method for opaque clouds, and by an infrared ratioing method using 6.7 and 10.8 μm for semitransparent clouds.

1. Introduction

Clouds are of continual interest because they provide a visible indication of what is going on in the atmosphere. Clouds play an important role in the Earth's climate and could be a crucial factor in evaluating the strength of global warming (see, for example, Lindzen *et al.* 2001, Hartman and Michelsen 2002, Choi *et al.* 2005*a*, Choi and Ho 2006). Knowledge of such a role requires development of the observational techniques applied to precise satellite measurements. Remote sensing of cloud properties has been studied focusing largely on the applications of the spectral bands of onboard radiometers. In the past few years, cloud analysis techniques have been considerably improved with the advent of Moderate-resolution Imaging Spectroradiometer (MODIS) instruments. The MODIS provides information on a variety of cloud properties by using spectral radiances at 36 visible and infrared (IR) bands (King *et al.* 1997, Baum *et al.* 2000). The detection of cirrus clouds has been particularly enhanced in MODIS by incorporating a band at 1.38 μm, which lies in

*Corresponding author. Email: hoch@cpl.snu.ac.kr

the strong water absorption region (Ackerman *et al.* 1998, Choi *et al.* 2005*b*). Recently, the Spinning Enhanced Visible and InfraRed Imager (SEVIRI), loaded onto the Meteosat Second Generation (MSG), has also promoted enhanced cloud data that are retrieved from a total of 12 spectral bands.

Although MODIS provides advanced atmospheric information with a high spatial resolution of up to 0.25 km × 0.25 km, the data are temporally limited in application for severe weather forecasting because they are being provided by polar orbiting platforms (i.e. the Terra and Aqua satellites). Korea has been using the geostationary observation data from the Japanese Multi-functional Transport Satellite (MTSAT-1R), which succeeded the Geostationary Meteorological Satellite (GMS) series covering East Asia and the western Pacific regions. However, its hourly data do not fulfil forecasters' requirements, especially for a fast developing weather system such as a severe thunderstorm. In addition, the information attainable from MTSAT-1R is limited to conventional parameters such as cloud amount, cloud-top pressure (p_c), and ground temperature (T_g). Therefore, both frequent observations in near real-time and diversely retrieved atmospheric products have become a key requirement, particularly to forecast severe weather events such as approaching tropical cyclones and torrential downpours in and around the Korean peninsula.

The launch of the first Korean geostationary satellite, the Communication, Ocean and Meteorological Satellite (COMS), is planned for 2008. The COMS will carry a separate imager and ocean colour sensor for meteorological and oceanography missions, respectively. Although the operation for the COMS Imager is not fixed yet, it will certainly include a rapid scan mode that acquires data for a limited area with much higher sampling frequency than the MTSAT-1R, possibly eight times per hour (Ahn *et al.* 2005). The COMS Imager measures radiances in five bands centred at approximately 0.6, 3.7, 6.7, 10.8 and 12.0 μm (see table 1). Its intention is to provide data with spatial resolutions of 1 and 4 km for visible and IR channels, respectively. The five channels only contain a narrow range of atmospheric information, so some cloud properties available in the MODIS and SEVIRI would not be distinguishable because of the limited number of bands. In particular, the absence of some essential channels, such as 2.2, 8.7 and 13.4 μm, limits the accurate retrieval of cloud properties. The cloud analysis algorithm (CLA) optimized for the five channels is nevertheless designed as part of the meteorological data processing system for COMS. The CLA is mainly used to derive five cloud property parameters: cloud phase, cloud type, cloud optical thickness (τ_c), effective particle radius (r_e), and cloud-top properties.

Table 1. COMS spectral band number and bandwidth.

Band	Bandwidth, μm	Used in cloud analysis
1	0.55–0.80	CT, COT/ER
2	3.5–4.0	CT, COT/ER
3	6.5–7.0	CP, CTTP
4	10.3–11.3	CP, CT, COT/ER, CTTP
5	11.5–12.5	CP, CT

CT, cloud type; COT/ER, cloud optical thickness/effective particle radius; CP, cloud phase; CTTP, cloud-top temperature and pressure.

This paper describes the approach to derive four of these cloud properties, and excludes cloud type, which will be described elsewhere. As the COMS Imager data are not yet available, we use MODIS data as surrogates of the COMS Imager data and radiative transfer (RT) model simulations for the algorithm development. Section 2 presents MODIS cloud data and briefly explains RT models to simulate outgoing radiances variable for cloud conditions. The method of algorithm validation is also explained. Section 3 introduces a cloud phase scheme adding a 6.7-μm band as a substitute for the 8.7-μm band used in the MODIS trispectral cloud phase algorithm. Section 4 details the method to retrieve τ_c and r_e by 0.6-, 3.7- and 10.8-μm bands, and discussion focuses on the functional approach concerned with the removal of thermal components in the 3.7-μm band. Section 5 introduces a simple method to use the 10.8-μm brightness temperature ($BT_{10.8}$), and a ratioing method using the 6.7- and 10.8-μm bands to estimate cloud-top temperature (T_c) and pressure (p_c). Finally, concluding remarks are given in section 6.

2. Data and methodology

2.1 *Data*

The present study uses two kinds of MODIS data sets: level 1b calibrated radiance (MOD02) and cloud product (MOD06). MOD02 contains calibrated radiances located at all 36 MODIS channels (both visible and IR regions). The data in MOD02 have a $1\,km \times 1\,km$ nadir resolution. MOD06 includes various cloud properties whose items cover all CLA products. The items in MOD06 used in this study are cloud phase, τ_c, r_e, T_c and p_c. The cloud phase in MOD06 is derived from the IR trispectral algorithm using 8.7-, 10.8- and 12.0-μm bands at $5\,km \times 5\,km$ nadir resolution. The algorithm operates on different absorption characteristics of ice and water clouds within the 8.5–13 μm region: the absorption ratios of the outgoing terrestrial radiation due to ice and water clouds are nearly equal within the 8.5–10 μm bands but diverge within the 10–13 μm bands (refer to Baum *et al.* 2000 for details). The total-column τ_c and r_e in MOD06 is determined by the combination of visible channels (0.6, 0.8 or 1.2 μm) and a near-IR channel (2.1 μm) at $1\,km \times 1\,km$ nadir resolution (refer to King *et al.* 1997 for details). T_c and p_c in MOD06 have the same resolution as the cloud phase (i.e. $5\,km \times 5\,km$); they are retrieved by a CO_2 slicing method (also called the radiance ratioing method) developed by Menzel *et al.* (1983). This method uses MODIS CO_2 absorption channels within 13.2–14.4 μm (i.e. MODIS bands 33, 34, 35 and 36). Besides cloud properties, MOD06 has angular parameters such as the satellite zenith angle (θ), the solar zenith angle (θ_0) and the azimuthal angle of the satellite relative to the sun (ϕ).

The 169 MODIS granules (5-min data) were collected for the mid-latitudes and the tropics during the period 1–16 March 2000. The radiances and angular parameters are used as inputs of the CLA. For this purpose, we chose 0.6 (MODIS band 1), 3.7 (band 20), 6.7 (band 27), 10.8 (band 31) and 12.0-μm (band 32) radiances (or converted BTs at $5\,km \times 5\,km$). The bands were chosen as they corresponded to COMS. The MODIS band filters are finer than those of COMS. This difference in bandwidths between MODIS and COMS may affect the estimation of the exact cloud properties. However, an advantage of using MODIS radiances is the capability to compare COMS-derived cloud properties with MODIS-derived cloud data (MOD06) on the pixel scale.

2.2 *Radiative transfer model*

To design the CLA with five channels, our study used the discrete ordinates radiative transfer (DISORT) models Streamer (Key and Schweiger 1998) and SBDART (Santa Barbara DISORT Atmospheric Radiative Transfer; Ricchiazzi *et al.* 1998). The spectral resolutions of the Streamer and SBDART models are $20\,\text{cm}^{-1}$ bandwidth in both short- and long-wave. A characteristic of the DISORT models is that the atmosphere is composed of a discrete number of adjacent, homogeneous layers. The single-scattering albedo and optical thickness are constant within each layer but may vary from layer to layer (Baum *et al.* 2000).

Although only one model should be dealt with for consistency of simulation, two models were used for different purposes because of their flexibility with regard to physical cloud properties. In addition, the Streamer exhibits a number of problems simulating radiance for near-IR bands (3.4–4.0 μm) (Key 2002). The Streamer was therefore used for cloudy conditions with varying cloud phase, T_c and p_c, while the SBDART was used for τ_c and r_e. Both models were used to calculate the top-of-atmosphere (TOA) radiances expected for clear and cloudy conditions. As the exact response functions of the COMS Imager channels are unknown at this point, we used the MTSAT-2 values as surrogates. Although they are not the same as the COMS Imager, it is expected that the difference would be very small because the specification and design of the two sensors are almost the same. In the Streamer, the temperature, humidity and ozone profiles for mid-latitude winter and summer, the polar region, and the tropics compiled by Ellingson *et al.* (1991) were used. In the SBDART, the atmospheric profiles (McClatchey *et al.* 1972) for mid-latitude winter were used. This is because input radiances for the CLA were obtained mainly over the mid-latitudes in winter. Aerosol contributions were neglected in this study.

2.3 *Validation*

The results of the CLA were verified by using the MODIS data and the RT models. The validation of the CLA was carried out for the following cloud properties: cloud phase, τ_c, r_e and p_c. The cloud phase was initially obtained by the CLA and consists of the thresholding tests inputting MODIS BTs. The retrieved cloud phase was simply compared with that of MODIS. For τ_c, r_e and p_c, the simulation of the RT model was prior to comparison with those of MODIS. For this purpose, TOA radiances were calculated by the RT model for the response function and the wavelengths corresponding to MODIS (i.e. MODIS bands 1, 20, 27, 31 and 32), because MODIS radiances were used as input radiances for the CLA.

3. Cloud thermodynamic phase

The discrimination of the cloud thermodynamic phase (i.e. ice or water) is of primary importance because it is a decisive factor in providing the radiative features of the cloud before retrieving any other cloud properties (Key and Intrieri 2000). In the current MODIS instruments, cloud phase was retrieved based on the IR trispectral method using bands at 8.7, 10.8 and 12.0 μm, as described by Strabala *et al.* (1994). Differences in the bulk and single-scattering properties of water droplets and ice crystals establish the basis of the IR trispectral method (Baum *et al.* 2000). The absorptivity increases more between 8 and 11 μm than between 11 and 12 μm for ice, but the opposite is true for water (refer to figure 1 of Baum *et al.* 2000). Consequently, the brightness temperature difference (BTD) values of ice

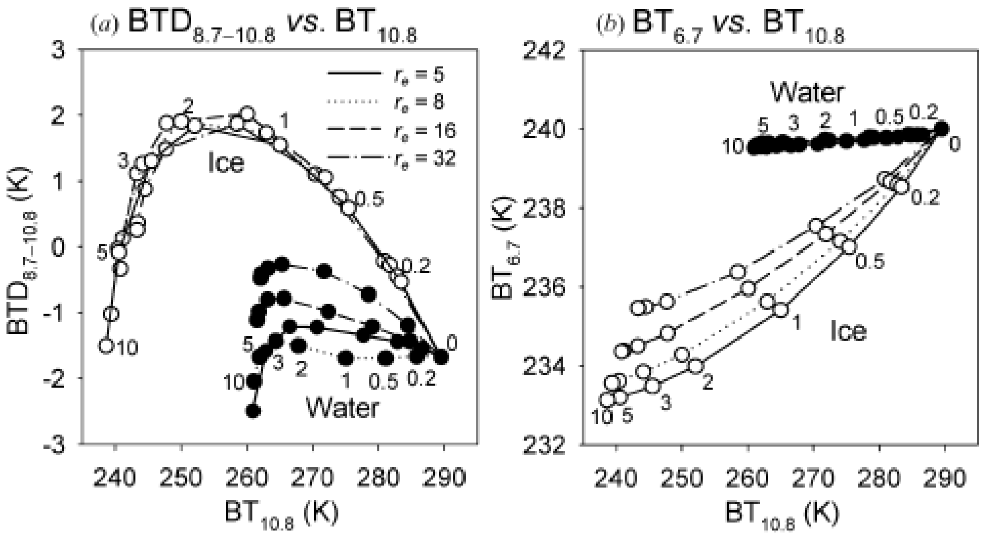

Figure 1. The results of an RT model simulation for (*a*) $BT_{10.8}$ *vs.* $BTD_{8.7-10.8}$ and (*b*) $BT_{10.8}$ *vs.* $BT_{6.7}$ for clouds composed of water droplets (filled circles) and ice crystals (open circles). The numbers indicate cloud optical thickness.

clouds between 8.7 and 10.8 μm ($BTD_{8.7-10.8}$) are greater than between 10.8 and 12.0 μm ($BTD_{10.8-12.0}$), whereas water clouds have greater $BTD_{10.8-12.0}$ than $BTD_{8.7-10.8}$ values.

The foregoing IR trispectral method in fact requires an 8.7-μm band, which plays an essential role in discriminating cloud phase, in cooperation with a 10.8-μm band. However, the 8.7-μm band is not a component band in most geostationary meteorological satellites except the MSG. The determination of cloud phase by applying 3.7-μm, in addition to 10.8- and 12.0-μm bands, was noted by Key and Intrieri (2000) for the case of a nonexistent 8.7-μm band in the Advanced Very High Resolution Radiometer (AVHRR) of National Oceanic and Atmospheric Administration (NOAA) satellites. However, the 3.7-μm band used on their method is affected by many factors including viewing/illumination geometry, surface reflectance, T_c and T_g. The present study attempted to use a 6.7-μm band instead. The 6.7-μm band is known to be sensitive to water vapour in the atmospheric layer between approximately 200 and 500 hPa, and the $BT_{6.7}$ has a lower value when high clouds exist in the layer (Ackerman *et al.* 1998). This suggests that $BT_{6.7}$ could be used to obtain information on the ice/water phase confined to high clouds.

Figures 1(*a*) and 1(*b*) show the RT model Streamer calculation of $BTD_{8.7-10.8}$ and $BT_{6.7}$ versus $BT_{10.8}$, respectively, at the TOA for single-layer ice and water clouds. The spectral BTs in the ice cloud are simulated with spherical particles for ice crystals. The assumption that ice crystals behave as spheres may be flawed because the high ice clouds include ice crystals of many different shapes (Takano and Liou 1989). However, it is known that scattering in the longwave is secondary to absorption (Pavolonis and Heidinger 2004). The calculation was carried out under various τ_c from 0 to 10 (numbers marked on the graphs) and r_e at 5, 8, 16 and 32. Water (ice) clouds are assumed to have a p_c of 500 hPa (300 hPa) under the standard profiles of mid-latitude summer (Ellingson *et al.* 1991), so that the simulation represents minimum (maximum) values for water (ice) clouds. The cloud water (ice)

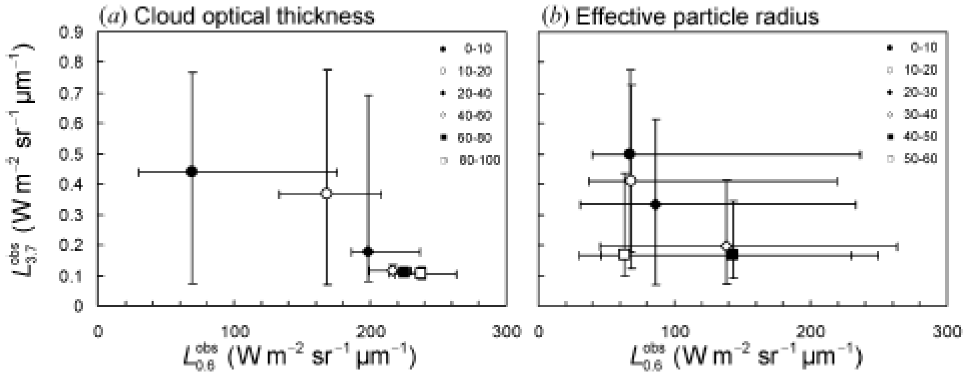

Figure 2. MODIS-retrieved cloud optical thickness (*a*) and effective particle radius (*b*) with respect to both 0.6- and 3.7-μm radiance taken from the MODIS observations. The error bars designate the minimum or maximum radiance for the corresponding τ_c and r_e.

content was set to 0.2 (0.02) g m^{-3}. In figure 1(*a*), ice clouds can have BTD$_{8.7-10.8}$ greater than about zero regardless of their effective radius, while water clouds cannot. This is consistent with the results of Baum *et al.* (2000) (see their figure 2). Likewise, ice clouds have BT$_{6.7}$ less than 239 K, whereas water clouds have BT$_{6.7}$ above 239 K (figure 1(*b*)). This difference in relation to values of BT$_{6.7}$ between water and ice clouds can be used to discriminate the cloud phase. BT$_{10.8}$ of 290 K and BT$_{6.7}$ of 240 K are maximal values corresponding to the cloud-free scene (τ_c=0) under the specific conditions: the T_g (=293 K), ground albedo (A_g=0.1) and the profiles of mid-latitude summer. To clarify the values of BT$_{10.8}$ and BT$_{6.7}$ as seen from the satellite, we further investigated the MODIS data collected in this study.

The relationships between cloud phase and BTD$_{8.7-10.8}$, BT$_{10.8}$ and BT$_{6.7}$ were examined by using the MODIS data. The relationship between the MODIS cloud phase and BTD$_{8.7-10.8}$ (or BT$_{10.8}$) is of course discrete because it is an ice or water phase in those tests. Clouds identified as being in the ice phase have a BTD$_{8.7-10.8}$ above 0.5 K (or a BT$_{10.8}$ below 238 K). This study also noted a relationship between the MODIS cloud phase and BT$_{6.7}$, which is also clear but not as distinct as that with BTD$_{8.7-10.8}$ (or BT$_{10.8}$) (data not shown here). Ice clouds identified by the MODIS algorithm tend to have a BT$_{6.7}$ up to about 250 K. Note that clouds identified as water and mixed phases can also have a BT$_{6.7}$ between 234 K and 250 K. Consequently, all the types of cloud phases in the MODIS data appear to take similar values of BT$_{6.7}$ between 234 K and 250 K.

Based on the results of both the RT calculation and the examination of the MODIS data, the algorithm for the cloud phase was recomposed, as described in table 2. The algorithm consists of the phase criteria from ice to unknown phase. The BT$_{10.8}$ and BTD$_{10.8-12.0}$ tests are applied from the IR trispectral method of the MODIS. The BT$_{6.7}$ test is combined with the BT$_{10.8}$ (or BTD$_{10.8-12.0}$) test at each

Table 2. The criteria for determining cloud phase.

Ice	Mixed	Water
BT$_{10.8}$<238 K or BTD$_{10.8-12.0}$≥4.5 K or BT$_{6.7}$<234 K	For no ice 238 K ≤ BT$_{10.8}$<268 K or 234 K ≤ BT$_{6.7}$<250 K	For no ice/mixed BT$_{10.8}$≥285 K or BT$_{6.7}$≥250 K

stage of phase decision (table 2). In detail, cloud pixels pass the stage of the ice phase decision first. At this stage, the three tests judge whether the pixel is composed of ice particles or not. If the pixel is not identified as ice, it passes on to the next tests using $BT_{10.8}$ and $BT_{6.7}$ for the mixed phase. If the pixel does not satisfy the criteria of being in the mixed phase, it will go through to the next stage using $BT_{10.8}$ and $BT_{6.7}$ for the water phase. Finally, the pixel unclassified as any phase category will be assigned to an unknown phase.

An effect of missing an 8.7-μm band in the IR trispectral method of the MODIS can be found by comparison of the MODIS cloud phase with that which has been newly retrieved by a $BT_{8.7}$-free algorithm (i.e. only using 10.8 and 12.0 μm). Table 3 shows that a large portion of the ice clouds are not well distinguished by the $BT_{8.7}$-free algorithm; the MODIS ice phase takes 40.8% of the total clouds whereas that from the $BT_{8.7}$-free algorithm takes only 15.6%. Moreover, the MODIS ice phase is in less agreement with that from the $BT_{8.7}$-free algorithm (15.6% in table 3). More than half of the scenes identified as ice clouds in MODIS are distinguished as mixed phases in the $BT_{8.7}$-free algorithm (21.2% *vs.* 40.8% in table 3).

The effect of adding a 6.7-μm band to the $BT_{8.7}$-free algorithm was also examined in a similar manner, and the results are presented in parentheses in table 3. It can be seen that the MODIS ice phase pixels are easily detected in the $BT_{6.7}$ algorithm (i.e. using 6.7, 10.8 and 12.0 μm). Specifically, MODIS data on detection of ice pixels are in 29.6% agreement with those from the $BT_{6.7}$ algorithm, which takes 72.5% of the total MODIS ice phase. The total percentage of ice phase increased up to 32.5%. This is a considerable improvement compared to the results from the previous $BT_{6.7}$-free algorithm. Those results account for the fact that large cloud regions comprising ice particles can be identified more accurately by their low $BT_{6.7}$ values, although cloud phases over the regions are not distinguishable through the $BT_{10.8}$ and $BTD_{10.8-12.0}$ threshold tests. Thus, detection of the ice phase using only $BT_{10.8}$ and $BT_{12.0}$ can cause serious problems in that a large portion of such ice clouds can be overlooked. To summarize, we have demonstrated that the 6.7-μm band can be a useful alternative in the case of a missing 8.7-μm band.

4. Cloud optical thickness (τ_c) and effective particle radius (r_e)

Since the determination of the scaled τ_c using a nonabsorbing visible wavelength 0.6-μm band was introduced by King (1987), the method has been used operationally for GMS-5 (Okada *et al.* 2001). τ_c is solely retrieved by this method because the near-IR channel is not available. Here, GMS-5 assumed the effective particle radius

Table 3. Comparison of cloud phase from the MODIS IR trispectral algorithm and from the algorithm for the COMS, as described in table 2. The numbers (in parentheses) designate those from the algorithm from which $BT_{6.7}$ is excluded (included).

	MODIS					
COMS	Clear	Water	Mixed	Ice	Uncertain	Total
Clear	13.0	0.0	0.0	0.0	0.0	13.0
Water	0.0	11.5 (19.7)	0.0	0.1 (0.3)	0.9 (4.1)	12.5 (24.1)
Mixed	0.0	2.3 (2.2)	7.1 (5.5)	21.2 (8.4)	5.8 (5.1)	36.4 (21.2)
Ice	0.0	0.0 (0.3)	0.0 (1.6)	15.6 (29.6)	0.0 (1.0)	15.6 (32.5)
Uncertain	0.0	13.8 (3.9)	0.0	3.9 (2.5)	4.9 (2.9)	22.6 (9.3)
Total	13.0	27.7	7.1	40.8	11.5	100.0

of all clouds to be 10 μm. Later, the retrieval method for both τ_c and r_e (also called the sun reflection method) was developed by combining water-absorbing near-IR wavelengths such as 1.6, 2.2 and 3.7 μm with the reflected radiance at 0.6 μm (Nakajima and King 1990, Nakajima and Nakajima 1995 (hereafter NN), and many other studies). Unlike 1.6 and 2.2 μm, however, the radiance at 3.7 μm contains large thermal components emitted from both the surface and the cloud top. The removal of the thermal components leads to importing other variables such as T_g and T_c, so that the accuracy of the products may decrease depending on these factors. For that reason, the algorithm of MODIS uses the near-IR 2.2 μm band, which is free of such components, together with visible 0.6 or 0.8 μm (King *et al.* 1997).

Although a 3.7-μm band has undesirable components for the sun reflection method, retrieval of τ_c and r_e by making use of 0.6 and 3.7 μm seems to be practical. Figures 2(*a*) and 2(*b*) show the dependence of MODIS-retrieved τ_c and r_e, respectively, on both 0.6- and 3.7-μm radiances. The 30 000 observed radiances over the ocean obtained in this study were plotted after being classified by the coincident values of τ_c and r_e. In figure 2, the various symbols correspond to the radiance averages for each τ_c and r_e category, and the error bars show the ranges of the radiance that each of τ_c and r_e categories can have. The pixels used in figure 2 are constrained to have the same angular variables (θ, θ_0, ϕ) to avoid angular dependence on the radiance from the cloud layer with τ_c (or r_e). As mentioned above, MODIS-retrieved τ_c and r_e are values derived from mainly 0.6 μm (0.8 μm) and 2.2 μm over land (sea). Nevertheless, figure 2 clearly shows that the cloud with a larger τ_c (r_e) has a greater (smaller) 0.6-μm (3.7-μm) radiance.

Figure 3 shows the RT model SBDART simulation of clouds with a variety of τ_c and r_e for 0.6-, 1.6-, 2.2- and 3.7-μm radiances under the condition of specific angular variables. Similar figures are shown in many studies (e.g. NN, King *et al.* 1997). The sensitivity of the nonabsorbing and absorbing channels to τ_c and r_e is almost orthogonal for optically thick clouds ($\tau_c \geq 16$). For optically thin clouds ($\tau_c < 16$), the sensitivity of the 0.6-μm and 2.2-μm (or 3.7-μm) channels is more orthogonal than that of the 1.6-μm channel (figure 3). This orthogonality ensures independent retrieval of τ_c and r_e (King *et al.* 1992). However, the intensity (i.e. radiance) at 3.7-μm itself is 10 digits smaller in comparison to other absorbing channels. Thus, using 3.7 μm requires a highly sensitive manipulation to prevent a large uncertainty in the retrieved τ_c and r_e.

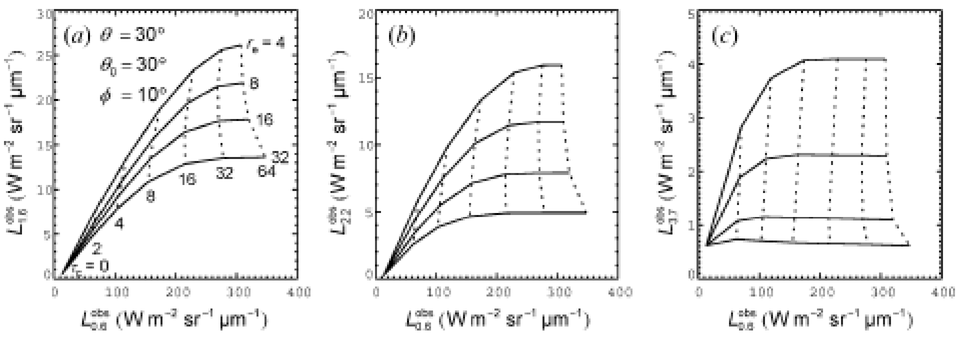

Figure 3. Comparison of (*a*) 1.6-, (*b*) 2.2- and (*c*) 3.7-μm radiances as a function of τ_c (0, 2, 4, 8, 16, 32, 64) and r_e (4, 8, 16, 32) with the angular variables of $\theta=30°$, $\theta_0=30°$ and $\phi=10°$.

The sun reflection method using 0.6 and 3.7 μm has been discussed previously by NN for the AVHRR. The method uses solar radiation only, reflected by cloud layer, and accompanies an essential process to undertake decoupling undesirable radiation components: (1) ground-reflected radiation, (2) cloud and ground thermal radiation. Based on the RT theory for plane-parallel layers with an underlying Lambertian surface (refer to NN), the decoupled radiances for 0.6- and 3.7-μm wavelengths are given simply as follows:

$$L_{0.6} = L_{0.6}^{\text{obs}} - L_{0.6}^{\text{sr}} \tag{1}$$

$$L_{3.7} = L_{3.7}^{\text{obs}} - L_{3.7}^{\text{sr}} - L_{3.7}^{\text{th}} \tag{2}$$

where L^{obs} is the satellite-received radiance, L^{sr} the ground-reflected radiance, and L^{th} the cloud and ground thermal radiance. The radiance is a function of τ_c, r_e, θ, θ_0 and ϕ. The cloud fraction reduces L^{obs} if a pixel is partially cloudy, which will consequently cause an underestimation of τ_c. Because there is not yet any method for completely picking out such partial-cloudy pixels, we assume that cloudy pixels are fully overcast in equations (1) and (2). NN designed an iterative algorithm that starts from initial values such as τ_c=35, r_e=10 μm and Z=2 km, where Z is the cloud-top height. They used preprocessed data; cloud-reflected radiance and reflectivity (at 0.6 and 3.7 μm), and transmissivity (at 0.6, 3.7 and 10.8 μm) (see NN for details). In brief, their algorithm compared model radiance with calculated radiance (observed radiance minus undesirable components), and it was iterated until exact values of τ_c and r_e were found.

This method is certainly applicable to the COMS algorithm because it has all the channels needed. However, the NN method requires too many assumptions to compute the undesirable components, as follows. First, cloud geometric thickness (D) is obtained from the relation $D= W/w$, where W and w are, respectively, the liquid water content and the liquid water path. In this calculation, W is led by the assumed formation (equation (11) of NN), and climatological w is simply used for five classified cloud types. At this point, cloud types must be an input, which complicates the algorithm. Second, Z is obtained by an assumed relationship with a constant lapse rate of 6.5 K km^{-1}. Third, 10.8-μm transmissivity (t) is derived with Z and the estimated D by a pre-calculated lookup table. Here, the use of a lookup table, as well as two other lookup tables, can increase numerical uncertainty. Fourth, T_g must be determined together with A_g, then T_c is determined with the previously derived T_g, A_g and t. Here, T_g for a cloud-free pixel adjacent to the target cloudy pixels may be another source of uncertainty in the calculation of T_c when clouds cover a large area.

To overcome those limitations, we did not carry out the calculation of D with initial Z or that of t, T_g and T_c, which were necessary parameters to get the undesirable radiation components in NN's method. Instead, observed radiances were explicitly decoupled from undesirable radiation components that were estimated by the direct use of climatological A_g and 10.8-μm radiance by equations (3) and (4), respectively. Ground-reflected radiance L_i^{sr} at i channel (e.g. 3.7 or 10.8 μm) can be estimated by

$$\begin{aligned} L_i^{\text{sr}} &\cong A_g L_i^{\text{sr}}(A_g=1) \\ &= A_g\left[\left(L_i + L_i^{\text{sr}}(A_g=1)\right) - \left(L_i + L_i^{\text{sr}}(A_g=0)\right)\right] \end{aligned} \tag{3}$$

where the multiple reflection between the ground surface and the upper layer is assumed to be very small, then L_i^{sr} changes almost linearly in proportion to A_g according to the RT theory applied to equations (1) and (2). We can further derive an extended formula, as shown in figure 3, with respect to thermal-free radiance, which is the sum of cloud- and ground-reflected radiances ($L_i + L_i^{sr}$). Note that L_i^{sr} is zero for A_g=0 and that L_i is cancelled out in the extended formula of equation (3). The RT simulation results in figures 2 and 3 of NN supporting the linear increase of thermal-free radiance at both 0.6- and 3.7-μm bands. On the basis of the extended form of equation (3), we can use only one lookup table, which contains the angular variables and their corresponding thermal-free radiances for two reference values of A_g (0 and 1) and for a variety of τ_c (0 to 64) and r_e (0 to 32 μm). Once angular variables and A_g are known, the simulated thermal-free radiance for A_g=0 is subtracted from that for A_g=1 in the lookup table and multiplied by a given A_g (equation (3)).

Cloud and ground thermal radiance at 3.7 μm is obtained from the following:

$$L_{3.7}^{th} \cong a \cdot L_{10.8}^{obs} 2 + b \cdot L_{10.8}^{obs} + c \qquad (4)$$

where $L_{10.8}^{obs}$ is the 10.8-μm satellite-received radiance, and a, b and c are regression coefficients. Equation (4) is based on the hypothesis that both $L_{3.7}^{th}$ and $L_{10.8}^{obs}$ are proportional to the Planck function of T_g and T_c. In this relationship, the different transmissivities of the atmosphere and the cloud layer, and a ground emissivity between 3.7 and 10.8 μm, would give rise to regression errors as shown in figure 4. The figure shows the result of the SBDART calculation for the sensitivity of the thermal radiance $L_{3.7}^{th}$ to $L_{10.8}^{obs}$. The calculations are carried out for clouds with a variety of τ_c (0–64) and r_e (0–32 μm) under diverse T_c (220–290 K) and T_g (250–300 K). The value of $L_{3.7}^{th}$ increases with the second-order polynomial relation when $L_{10.8}^{obs}$ increases. The mean error range of $L_{3.7}^{th}$ for all the $L_{10.8}^{obs}$ values is about 0.02 W m^{-2} μm^{-1} sr^{-1}, which causes 2% uncertainty in the final r_e. In addition, this

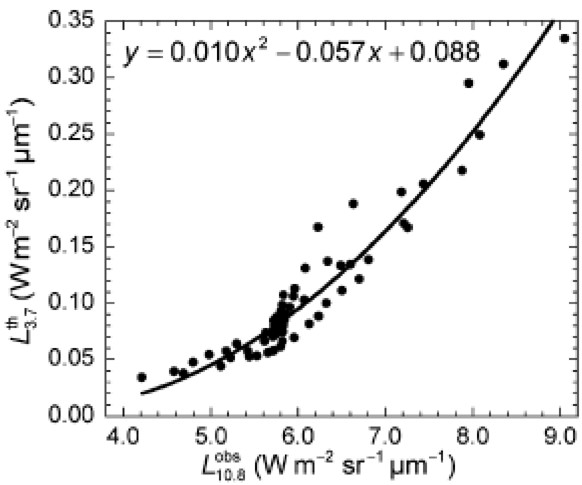

Figure 4. Sensitivity of 3.7-μm thermal radiances ($L_{3.7}^{th}$) to 10.8-μm satellite-received radiances ($L_{10.8}^{obs}$) for the clouds with a variety of τ_c (0 to 64) and r_e (0 to 32 μm) under diverse T_c and T_g. The solid line is the second-order polynomial regression line of the plots.

decoupling method indicates, in figure 4, that the error of $L_{3.7}^{\mathrm{th}}$ would be even larger for cold surfaces (i.e. cold $L_{10.8}^{\mathrm{obs}}$). Taking into account the fact that NN's method needed many lookup tables to obtain the thermal radiance as a function of many factors such as cloud albedo, t, A_g, T_g and T_c, the decoupling method using such a simple relationship between $L_{3.7}^{\mathrm{th}}$ and $L_{10.8}^{\mathrm{obs}}$ is fairly effective in time. Finally, we removed undesirable components from the observed radiance by equations (1) and (2) with the aid of equations (3) and (4).

Figures 5(*a*) and 5(*b*) respectively show a comparison of τ_c and r_e from the new algorithm with those of MODIS. τ_c from the new algorithm is in fairly good agreement with MODIS τ_c for optically thin clouds (τ_c<20). For thick clouds, τ_c deviates even more from the linear relationship (figure 5(*a*)). The mean root-mean-square errors of τ_c for thin and thick clouds are 1.39 and 5.38, respectively. This low accuracy for thick clouds results from $L_{0.6}$ itself increasing slightly for a constant r_e when the τ_c increases above 20, as shown in the RT result of figure 3. However, r_e from the new algorithm is in accord with MODIS r_e for small particles (r_e<12 μm). For large particles, the deviation in r_e is increased for similar reasons to those stated above for τ_c. Namely, $L_{3.7}$ itself decreases slowly when r_e increases above about 12 μm (see figure 3). The mean root-mean-square errors in r_e for small and large particles are 0.83 and 1.76 μm, respectively (figure 5(*b*)).

5. Cloud-top temperature (T_c) and pressure (p_c)

The IR-window channel estimate is the typical method in which $BT_{10.8}$ is compared with a vertical temperature profile in the area of interest. It is assumed that the cloud is opaque and fills the field of view (FOV). This is inaccurate for semi-transparent cirrus and small-element cumulus clouds (Menzel *et al.* 1983). To obtain the criterion of τ_c proper for the IR-window channel estimate, we simply depict $BT_{10.8}$ and T_c in MODIS (figure 6). Here, it is clear that T_c of an optically thick cloud (τ_c>10) has a nearly linear relationship with its $BT_{10.8}$. For the same angular conditions, an optically thick cloud with a lower T_c theoretically emerges with a

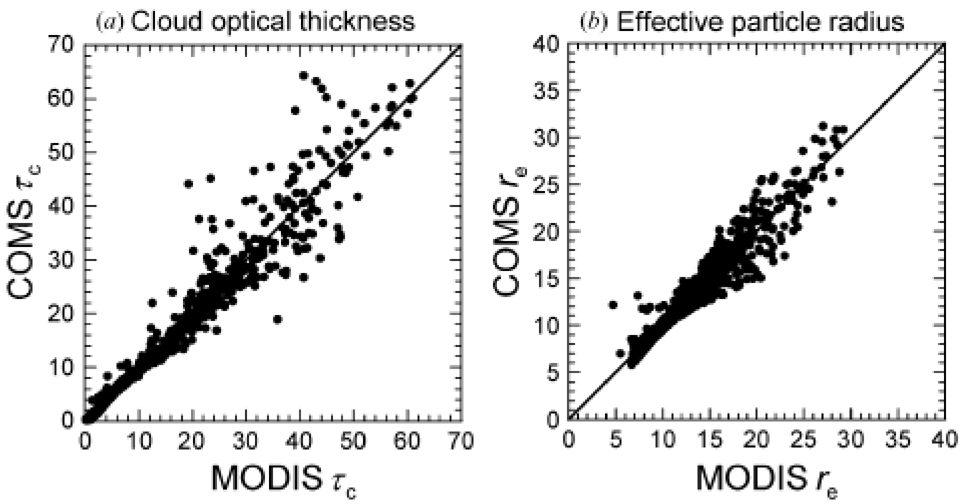

Figure 5. Comparison between MODIS-retrieved and COMS-retrieved (*a*) cloud optical thickness (τ_c) and (*b*) effctive particle radius (r_e).

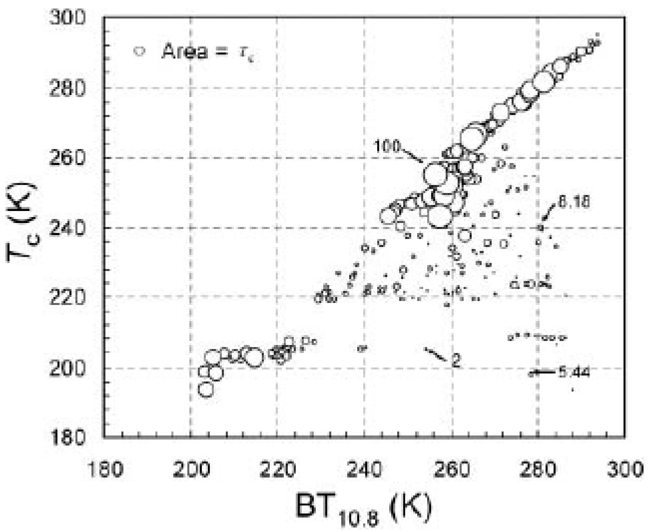

Figure 6. Scatter plots depicted from MODIS-retrieved T_c and its corresponding $BT_{10.8}$ for clouds (τ_c>2). The circles are sized by cloud optical thickness.

lower radiance at 10.8 μm. The $BT_{10.8}$ from the high semitransparent clouds is generally contaminated by underlying clouds or surfaces. This is shown by the fact that $BT_{10.8}$ is greater than T_c in figure 6. To alleviate this discrepancy, a radiance rationing method has been developed and used for operational purposes (see, for example, Smith and Platt 1978, Menzel *et al.* 1983).

The idea of using the ratio of the cloud signal for two CO_2 channels viewing the same FOV to determine the p_c appeared in Smith and Platt (1978). Menzel *et al.* (1983) further described this method in detail. Wylie *et al.* (1994) used this method to determine cirrus cloud statistics from NOAA's polar-orbiting High-Resolution Infrared Radiation Sounder multispectral data in terms of cloud cover, height and effective emissivity. The window channel has also been involved in the radiance ratioing method together with the sounding channels (6.2, 7.3 and 13.4 μm) to retrieve the p_c of thin clouds for SEVIRI (Le Gléau 2005).

The COMS Imager has limited channels for importing the radiance ratioing method, so that only the IR-window channel (10.8 μm) and one sounding channel (6.7 μm) are available. Thus, it is necessary to evaluate this method with the two available channels. All the equations for this method are the same as those derived in Menzel *et al.* (1983). We show the relationship between the ratio ($G_{6.7}^{10.8}$) and p_c as follows.

$$G_{6.7}^{10.8}(p_c) \cong \frac{L_{10.8}^{\mathrm{cld}} - L_{10.8}^{\mathrm{clr}}}{L_{6.7}^{\mathrm{cld}} - L_{6.7}^{\mathrm{clr}}} \quad (5)$$

where L^{clr} and L^{cld} are the radiances of clear-sky and cloudy-sky, respectively. We assumed here that cloud emissivities at the two channels are near unity. It should be noted that 6.7-μm is a strong water vapour absorbing channel, so that its maximum value of weighting function is located at an altitude of around 400 hPa. Thus, $G_{6.7}^{10.8}$ in equation (5) can be applied only to high clouds with $p_c \leqslant 400$ hPa. Multilayer cloud systems in which an upper semitransparent cloud layer exists over an underlying opaque cloud (p_c>500 hPa) layer will not lead to an overestimation of the p_c of the semitransparent cloud, contrary to the CO_2 slicing method of MODIS (King *et al.* 1992).

Figure 7 shows the RT model Streamer simulation of $G_{6.7}^{10.8}$ for single-layer ice clouds located at 200–400 hPa. This is calculated under the conditions of $\theta=30°$ for the tropical, mid-latitude and polar atmospheric profiles. The ice clouds are assumed to be composed of spherical particles. Each ratio is computed by the regression of 16 cases for various τ_c (0.5, 1, 2 and 5) and r_e (20, 50, 100 and 130). Clouds at 200, 300 and 400 hPa have distinct ratios of 13, 18 and 32 (18, 35 and 87) for mid-latitudes (the tropics). It is obvious that the ratio increases depending on p_c, except for the polar region. Standard errors ($\sigma/\sqrt{n}$) are 8.0, 2.1 and near zero for the tropical, mid-latitude and polar atmospheric profile, respectively (error bars in figure 7). In all the profiled cases, the correlation coefficients (between $L_{10.8}^{cld}-L_{10.8}^{clr}$ and $L_{6.7}^{cld}-L_{6.7}^{clr}$) for the regression have nearly constant values between 0.82 and 1.00 (not shown). These high correlations indicate that clouds at a specific altitude have an inherent ratio regardless of their diverse τ_c and r_e. In general, a lower cloud in the tropics tends to have a smaller correlation value because water vapour in the atmosphere absorbs more 6.7-μm radiance from lower clouds.

The satellite zenith angle θ is also an important component to be considered for the calculation of $G_{6.7}^{10.8}$ in equation (5), while other angles such as θ and ϕ relative to the sun do not affect the 6.7-μm radiance. Table 4 shows the dependence of the ratios on various θ (0, 30 and 60) for mid-latitude winter. The ratio is greater for lower cloud regardless of θ. Here, all the ratios are calculated with a correlation coefficient of more than 0.93. It has also been found that a greater value of the ratio is computed for larger values of θ for the same p_c.

The choice of an appropriate clear-sky radiance is an important issue, as indicated in equation (5). The ratio from the measured radiance must be well matched with the pre-calculated ratio from the RT model in operational T_c and p_c retrievals. If the

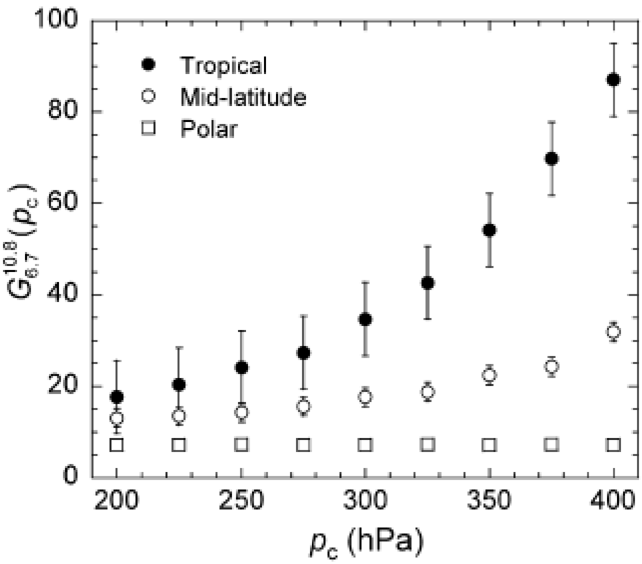

Figure 7. Simulation of radiance ratio ($G_{6.7}^{10.8}$) for single-layer ice clouds (at 200–400 hPa) under the condition of $\theta=30°$ for the tropical (solid circles), mid-latitude (open circles), and polar atmospheric profiles (open squares). Values are plotted with standard errors ($\sigma/\sqrt{n}$).

Table 4. Ratios ($G_{6.7}^{10.8}$) calculated for various satellite scan angles (θ). This simulation was performed for clouds at 200, 300 and 400 hPa and for mid-latitude winter.

θ (deg)	200 hPa	300 hPa	400 hPa
60	16.2	23.0	48.5
30	13.1	17.7	31.9
0	12.4	16.6	28.9

ratio is calculated with improper clear-sky radiance for a cloudy FOV, it leads to serious uncertainty in T_c and p_c. COMS CLA takes up the method in which we find a maximum of clear-sky radiance between observed pixels adjacent to cloudy pixels in the 50 km × 50 km FOV and simulated by the RT model with numerically predicted atmospheric profiles.

However, the MODIS current algorithm retrieves p_c by combining five ratios with MODIS CO_2 channels (G_{35}^{36}, G_{34}^{35}, G_{33}^{35}, G_{33}^{34} and G_{31}^{33}) after first estimates of the 10.8-μm radiance (Menzel *et al.* 2002). Here, G_{35}^{36} indicates the ratio using MODIS bands 36 and 35, in which the clear-sky radiance is obtained from the RT calculation with the aid of the National Centers for Environmental Prediction (www.cdc.noaa.gov). Therefore, the MODIS retrieval of p_c is accepted as the reference truth with an expected error of at least 50 hPa.

Figure 8 shows examples of the relationship between $G_{6.7}^{10.8}$ in the MODIS observation and the MODIS-retrieved p_c. $G_{6.7}^{10.8}$ values are simply calculated for each of the 5 × 5 pixels in the MODIS granules for 0155, 0200 and 0300 UTC of 4 March 2000, with the FOV covering Southeast Asia (13°–34° N, 113°–150° E), the tropical western Pacific (5° S–16° N, 119°–144° E) and Northeast Asia (27°–48° N, 100°–132° E), respectively (box plots in figure 8). In the calculation of $G_{6.7}^{10.8}$, the clear-sky radiance is chosen as the maximum value among clear-sky pixels in 5 × 5 pixels, and the cloudy-sky radiance as the mean value of four cloudy pixels in 5 × 5 pixels. Accordingly, the 5 × 5 pixels in this calculation must include at least one observed clear-sky pixel, which prevents bias in our analysis that may be caused when using RT-simulated clear-sky radiance as a substitute for observed clear-sky radiance. The cases in 5 × 5 pixels, however, are not completely reliable as they hold only about 1% of the total in a granule. It is found that the distribution and median of values of $G_{6.7}^{10.8}$ increase with increasing p_c as a whole, although they show considerable ranges of the values (figure 8). These large ranges may arise because the calculation allows the conditions of θ of 0° to about 60° and of atmospheric profiles differing among pixels.

To compare the foregoing observational results with the RT calculation, $G_{6.7}^{10.8}$ is simulated by the Streamer in a manner similar to that shown in figure 7, but with the mean atmospheric profile in the granule under the conditions of 0° (solid circles) and 60° (open circles) in figure 8. Here, we used coincident retrieved atmospheric profiles with the ratio, which are provided in the MODIS atmospheric profile product (MOD07). This figure does not show the ratio induced by the regression analysis with correlation lower than 0.6 (clouds at lower than 325 hPa in figures 8(*a*) and 8(*b*)). The deviation between the MODIS observation and the RT calculation remains, as the atmospheric profile applied to the RT model is a mean value and may not be the exact truth (figures 8(*a*–*c*)). Water vapour contaminates the 6.7-μm radiance emitted from the cloud top below an altitude of 350 hPa even more than that from a higher cloud top in both the observation and RT calculation,

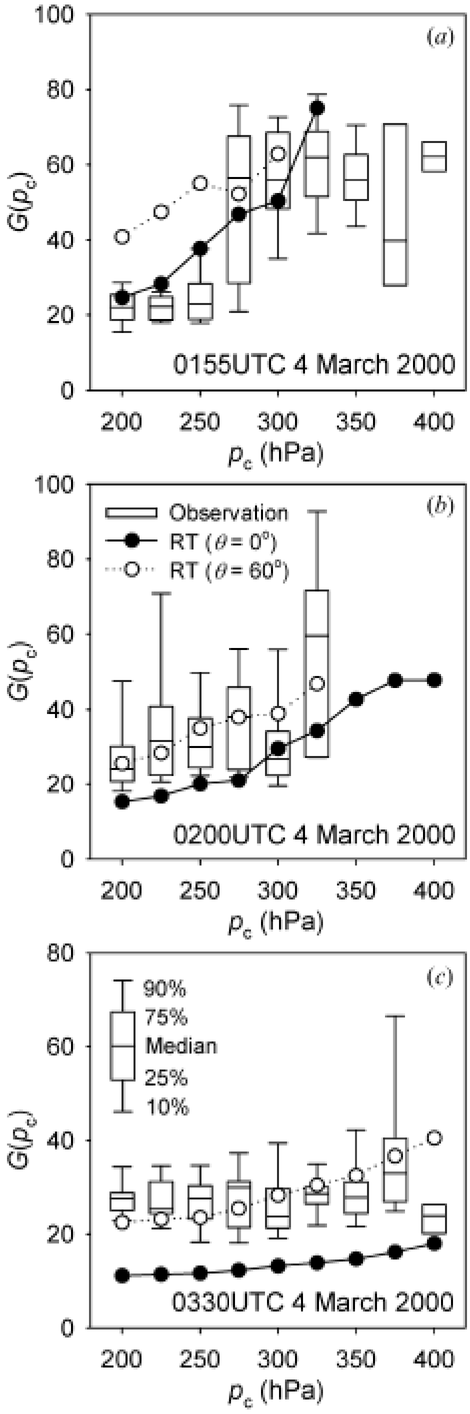

Figure 8. Box plot summing up the distribution, median and variability of radiance ratio ($G_{6.7}^{10.8}$) calculated from the MODIS granules for (*a*) 0155 UTC (13°–34° N, 113°–150° E), (*b*) 0200 UTC (5° S–16° N, 119°–144° E) and (*c*) 0330 UTC (27°–48° N, 100°–132° E) of 4 March 2000. The solid and open circles correspond to values of $G_{6.7}^{10.8}$ that are simulated by the RT model under the conditions of θ=0° and 60°, respectively, for the mean atmospheric profiles over each of the granules.

particularly in the Tropics. Therefore, the observed $G_{6.7}^{10.8}$ and the RT result become ambiguous for clouds under 350 hPa (figures 8(*a*) and 8(*b*)). The large uncertainty for clouds under 350 hPa is relatively small in mid-latitude, but the derivative of the $G_{6.7}^{10.8}$ with respect to p_c is somewhat undersized (figure 8(*c*)). Consequently, the uncertainty seems to be inevitable in retrieving p_c by the ratio $G_{6.7}^{10.8}$ in at least 50 hPa, which corresponds to 3 K on average for inversed T_c.

6. Concluding remarks

The first Korean geostationary satellite, COMS, is scheduled to be launched in 2008. One of the most important meteorological mission objectives of COMS is to improve the prediction of severe weather events. The COMS Imager will have five channels at 0.6, 3.7, 6.7, 10.8 and 12.0 μm. This preliminary study suggests practical methods of retrieving cloud properties by fully utilizing the five channels of the COMS. The major characteristics of the methods are summarized as follows.

A new algorithm applying 6.7-μm in addition to 10.8- and 12.0-μm radiances has shown improved accuracy in the detection of the ice phase from the available data. This approach works comparatively well even in the absence of the 8.7-μm band, which is essential for the retrieval of the cloud phase in the MODIS IR trispectral algorithm.

The retrieval of τ_c and r_e using cloud-reflected 0.6- and 3.7-μm radiances is achieved by the rapid removal of undesirable radiance components. These components are obtained from a lookup table composed of angular variables, climatological A_g, and the 10.8-μm radiance measured for a coincident pixel. The τ_c (r_e) attained by this algorithm has shown a valid relationship, better below 20 (12 μm), than MODIS-retrieved τ_c (r_e) in its validation analysis using the available data.

The IR-window estimate using $BT_{10.8}$ was performed for the T_c and p_c of optically thick clouds (τ_c>10). The radiance ratioing method using 6.7- and 10.8-μm bands was introduced for optically thin high clouds (200–400 hPa). Contrary to the *in situ* methods using other sounding channels, it must consider two factors: θ and the atmospheric profile.

The limitations of the foregoing algorithm are the following. First, the ice phase can be overlooked for existing semitransparent clouds by this method of retrieval of the cloud phase. Thus, the method using $BT_{6.7}$ is efficient for most convective clouds. Second, the decoupling method slightly lowers the accuracy of τ_c and r_e. In particular, r_e can accumulate more noise by the additional removal of thermal components at 3.7-μm ($L_{3.7}^{th}$). As a result, the value of τ_c (r_e) over about 20 (12 μm) deviates more from the MODIS products. Third, the radiance ratioing method for T_c and p_c cannot be applied to clouds in polar regions. The performance of the method is relatively superior in the tropics, but clouds below 350 hPa are often contaminated by upper atmospheric moisture. The p_c estimated by this method presents a large bias compared with the MODIS-retrieved p_c. This bias may be lessened through an exact estimate of clear-sky radiance and an atmospheric profile.

Further studies remain to be performed on the validation of this method using MODIS data extended to other seasons. This should be carried out based on the conditions of abundant computer space and precise atmospheric profiles. There is also a need to perform a comparison of cloud products with similar data from other geostationary satellites and ground-based measurements collected at the Atmospheric Radiation Measurement Program. The influence of the lower radiometric accuracy of COMS compared to the MODIS may debase the validity of the COMS CLA algorithm. Consequently, other geostationary satellites with five channels similar to COMS (e.g. MTSAT-1R) are expected to give us successful results for a prototype validation. The ground-based observation is usually limited to the cloud base, but its cloud optical properties will be useful in any future validation.

Acknowledgements

This study was undertaken for the COMS project funded by the Korean Meteorological Administration. Y.-S.C. and Y.-M.K. are supported by the BK21 project of the Korean government. We thank an anonymous reviewer for valuable comments. The MODIS data were provided by the Earth Observing System Data and Information System, Distributed Active Archive Center, at Goddard Space Flight Center, which archives, manages, and distributes these data.

References

ACKERMAN, S.A., STRABALA, K.I., MENZEL, W.P., FREY, R.A., MOELLER, C.C. and GUMLEY, L.E., 1998, Discriminating clear-sky from clouds with MODIS. *Journal of Geophysical Research*, **103**, pp. 32141–32157.

AHN, M.H., SEO, E.J., CHUNG, C.Y., SOHN, B.J., SUH, M.S. and OH, M., 2005, Introduction to the COMS meteorological data processing system. In *International Symposium on Remote Sensing*, 12–14 October 2005, Jeju, Korea (Seoul: The Korean Society of Remote Sensing), pp. 95–97.

BAUM, B.A., SOULEN, P.F., STRABALA, K.I., KING, M.D., ACKERMAN, S.A., MENZEL, W.P. and YANG, P., 2000, Remote sensing of cloud properties using MODIS airborne simulator imagery during SUCCESS. 2. Cloud thermodynamic phase. *Journal of Geophysical Research*, **105**, pp. 11781–11792.

CHOI, Y.S., HO, C.H. and SUI, C.H., 2005a, Different optical properties of high cloud in GMS and MODIS observations. *Geophysical Research Letters*, **32**, L23823, doi: 10.1029/2005GL024616.

CHOI, Y.S., HO, C.H., AHN, M.H. and KIM, Y.S., 2005b, Enhancement of the consistency of MODIS thin cirrus with cloud phase by adding 1.6-μm reflectance. *International Journal of Remote Sensing*, **26**, pp. 4669–4680.

CHOI, Y.S. and HO, C.H., 2006, Radiative effect of cirrus with different optical properties over the tropics in MODIS and CERES Observations. *Geophysical Research Letters*, **33**, L21811, doi: 10.1029/2006GL027403.

ELLINGSON, R.G., ELLIS, J. and FELS, S., 1991, The intercomparison of radiation codes used in climate models: long wave results. *Journal of Geophysical Research*, **96**, pp. 8929–8953.

HARTMANN, D.L. and MICHELSEN, M.L., 2002, No evidence for iris. *Bulletin of the American Meteorological Society*, **83**, pp. 249–254.

KEY, J.R. and SCHWEIGER, A., 1998, Tools for atmospheric radiative transfer: Streamer and FluxNet. *Computers and Geosciences*, **24**, pp. 443–451.

KEY, J.R. and INTRIERI, J.M., 2000, Cloud particle phase determination with the AVHRR. *Journal of Applied Meteorology*, **39**, pp. 1797–1804.

KEY, J.R., 2002, *Streamer Version 3.0 User's Guide* (Madison, WI: NOAA/NESDIS). Available online at: stratus.ssec.wisc.edu.

KING, M.D., 1987, Determination of the scaled optical thickness of clouds from reflected solar radiation measurements. *Journal of the Atmospheric Sciences*, **44**, pp. 1734–1751.

KING, M.D., KAUFMAN, Y.J., MENZEL, W.P. and TANRE, D., 1992, Remote sensing of cloud, aerosol, and water vapor properties from the Moderate Resolution Imaging

Spectrometer (MODIS). *IEEE Transactions on Geoscience and Remote Sensing*, **30**, pp. 2–27.

KING, M.D., TSAY, S.C., PLATNICK, S.E., WANG, M. and LIOU, K.N., 1997, Cloud retrieval algorithms for MODIS: optical thickness, effective particle radius, and thermodynamic phase. In *MODIS Algorithm Theoretical Basis Document* (NASA).

LE GLÉAU, H., 2005, *Software User Manual of the SAFNWC/MSG: Scientific Part for the PGE01-02-03. SAFNWC Software V1.2.* Available online at: http://www.meteorologie.eu.org/safnwc/publis.htm, pp. 35–53. Meteo, France.

LINDZEN, R.S., CHOU, M.D. and HOU, A.Y., 2001, Does the earth have an adaptive infrared iris? *Bulletin of the American Meteorological Society*, **82**, pp. 417–432.

MCCLATCHEY R.A., FENN, R.W., J. SELBY, E.A., VOLZ, F.E. and GARING, J.S., 1972, *Optical Properties of the Atmosphere*, 3rd edn. AFCRL Environment Research Paper No. 411, (Bedford, Massachusettes: Cambridge Research Laboratory), p. 108.

MENZEL, W.P., SMITH, W.L. and STEWART, T.R., 1983, Improved cloud motion wind vector and altitude assignment using VAS. *Journal of Climate and Applied Meteorology*, **22**, pp. 377–384.

MENZEL, W.P., BAUM, B.A., STRABALA, K.I. and FREY, R.A., 2002, Cloud top properties and cloud phase. In *MODIS Algorithm Theoretical Basis Document* (NASA), ATBD_MOD_04, NASA Goddard Space Flight Center. Available online at: http://modis-atmos.gsfc.nasa.gov/MOD06_L21.

NAKAJIMA, T.Y. and KING, M.D., 1990, Determination of the optical thickness and effective particle radius of clouds from reflected solar radiation measurements, Part 1: Theory. *Journal of the Atmospheric Sciences*, **47**, pp. 1878–1893.

NAKAJIMA, T.Y. and NAKAJIMA, T., 1995, Wide-area determination of cloud microphysical properties from NOAA AVHRR measurements for FIRE and ASTEX regions. *Journal of the Atmospheric Sciences*, **52**, pp. 4043–4059.

OKADA, I., TAKAMURA, T., KAWAMOTO, K., INOUE, T., TAKAYABU, Y. and KIKUCHI, T., 2001, Cloud cover and optical thickness from GMS-5 image data. In *Proceedings GAME AAN/Radiation Workshop*, 8–10 March 2001, Phuket, Thailand (Nagoya: GAME International Project Office), pp. 9–11.

PAVOLONIS, M.J. and HEIDINGER, A.K., 2004, Daytime cloud overlap detection from AVHRR and VIIRS. *Journal of Applied Meteorology*, **43**, pp. 762–778.

RICCHIAZZI, P., YANG, S., GAUTIER, C. and SOWLE, D., 1998, SBDART: a research and teaching software tool for plane-parallel radiative transfer in the earth's atmosphere. *Bulletin of the American Meteorological Society*, **79**, pp. 2101–2114.

SMITH, W.L. and PLATT, C.M., 1978, Comparison of satellite-deduced cloud heights with indications from radiosonde and ground-based laser measurements. *Journal of Applied Meteorology*, **17**, pp. 1796–1802.

STRABALA, K.I., ACKERMAN, S.A. and MENZEL, W.P., 1994, Cloud properties inferred from 8–12-μm data. *Journal of Applied Meteorology*, **33**, pp. 212–229.

TAKANO, Y. and LIOU, K.N., 1989, Solar radiative transfer in cirrus clouds. Part I: Single scattering and optical properties of hexagonal ice crystals. *Journal of the Atmospheric Sciences*, **46**, pp. 3–19.

WYLIE, D.P., MENZEL, W.P., WOOLF, H.M. and STRABALA, K.I., 1994, Four years of global cirrus cloud statistics using HIRS. *Journal of Climate*, **7**, pp. 1972–1986.